

Neutron Stars

James M. Lattimer

Dept. of Physics & Astronomy
Stony Brook University
Stony Brook, NY 11794-3800
lattimer@astro.sunysb.edu

ABSTRACT

The structure, formation, and evolution of neutron stars are described. Neutron stars are laboratories for dense matter physics, since they contain the highest densities of cold matter in the universe. Combining laboratory experiments with observations of neutron stars will constrain the equation of state of relatively cold and dense matter. In addition, neutron stars are also laboratories for testing general relativity theory.

1. From Theory to Discovery

Soon after the discovery of neutrons themselves by Chadwick in 1932, neutron stars were first proposed by Landau who suggested that in analogy to the support of white dwarfs by electron degeneracy pressure, neutron stars could be supported by neutron degeneracy pressure. Baade and Zwicky¹ in 1934 first suggested neutron stars as being the remnants of supernovae. Tolman² in 1939 produced a major study of their theoretical structure, employing the relativistic equations of stellar structure following from Einstein's equations of general relativity. This work demonstrated, among other interesting ideas, that neutron stars could not be of arbitrarily large mass: general relativity introduces the concept of a neutron star maximum mass. Interestingly, the magnitude of the neutron star maximum mass is of the same order as the Chandrasekhar mass, which is the limiting mass for a white dwarf that exists in Newtonian gravity. Additional theoretical work followed, in which it was realized that neutron stars were likely to be rapidly rotating and to have intense magnetic fields. Pacini³ predicted that a rotating magnetized neutron star would emit radio waves. But it was not until the 1967 Bell and Hewish⁴ discovery of radio pulsars that the existence of neutron stars was put on firm ground. Gold⁵ quickly made the connection between the extremely regular observed pulsations and a model of a highly magnetized, rapidly rotating and extremely compact configuration.

The periods of pulsars range from seconds down to milliseconds. The rotation periods are observed to be extremely stable, with P/\dot{P} ranging from thousands to millions of years. The periods are observed to be generally increasing. These three facts virtually guarantee that one is dealing with the rotation of a massive object. The short periods imply that

the size of the pulsar is small. The distance cP is about 3000 km for $P = 0.01$ s. Unless relativistic beaming with $\gamma \sim 100$ is occurring, a compact star is required. Vibrations of a star are ruled out because, generally, as vibrations decay their period decreases. Furthermore, the characteristic vibrational frequency is $2\pi(G\rho)^{-1/2}$, only a few milliseconds, and is too short. Finally, pulsing due to two orbiting objects is ruled out by the prediction of general relativity that a close compact binary will emit gravitational radiation, which again decreases its period as the orbit decays.

A rotating rigid sphere with period P will begin to shed mass from its equator when the orbital period at the star's surface equals P . Thus the limiting period is defined by

$$\sqrt{\frac{GM}{R^3}} = \frac{2\pi}{P_{lim}}, \quad P_{lim} = 0.55 \left(\frac{M_{\odot}}{M}\right)^{1/2} \left(\frac{R}{10 \text{ km}}\right)^{3/2} \text{ ms.}$$

For a white dwarf, for example, the limiting rotational period would be of order 15 s. Only a neutron star can be more compact without forming a black hole.

Although the details of the generating mechanism are vague, it is believed that the pulsations of a neutron star can be understood in terms of the energetics of a rotating dipole. If the magnetic and rotation axes are not perfectly aligned, then a beam of radiation emanating from the magnetic axes will pierce the surrounding space like a lighthouse beacon. The torque exerted by the beam will slowly spin down the pulsar.

The magnetic moment magnitude of a sphere with a dipole field of strength B is

$$|\mathbf{m}| = BR^3/2.$$

If the magnetic field is not aligned with the rotation axis, the magnetic field will change with time and therefore energy will be radiated. The emission rate is

$$\dot{E} = -\frac{2}{3c^3}|\ddot{\mathbf{m}}|^2 = -\frac{B^2 R^6 \Omega^4}{6c^3} \sin^2 \alpha, \quad (1.1)$$

where $\Omega = 2\pi/P$ and α is the misalignment angle. Ultimately, the source of the emitted energy is the rotational energy,

$$E = \frac{1}{2}I\Omega^2, \quad \dot{E} = I\Omega\dot{\Omega} \quad (1.2)$$

where I is the moment of inertia of the pulsar. If the original spin frequency is Ω_i and the present frequency is Ω_0 , one finds for the present age of the pulsar

$$t = \frac{P}{2\dot{P}} \left[1 - \left(\frac{\Omega_0}{\Omega_i}\right)^2 \right]^{-1/2} \simeq \frac{P}{2\dot{P}}$$

where we assumed $\Omega_i \gg \Omega_0$ is the last step. We define $T = 2P/\dot{P}$ as the characteristic age of the pulsar. In a few cases in which the age of the pulsar can be independently determined by direct observation (such as for the Crab pulsar) or inferred from kinematics, the characteristic age is only accurate to factors of 3 or so. Eliminating \dot{E} from Eq. (1.1) by using Eq. (1.2), one finds that the orthogonal component of the magnetic field is

$$B \sin \alpha = 3 \times 10^{19} \sqrt{P\dot{P} \frac{I}{10^{45} \text{ g cm}^2}} \text{ G.} \quad (1.3)$$

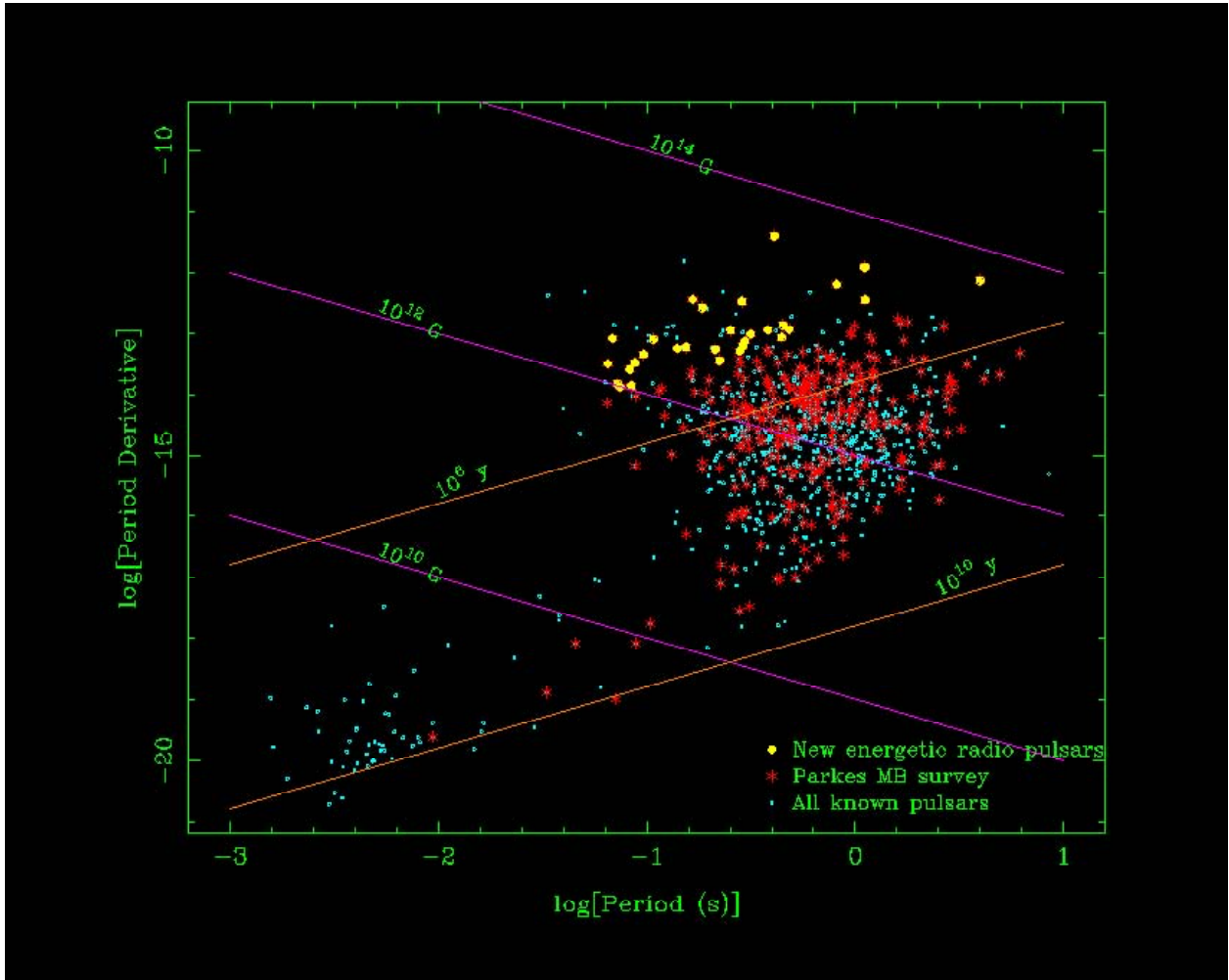


Figure 1.1: Period vs. period derivative for pulsars. Lines of constant characteristic age (red) and magnetic field strength (violet) are displayed. Generally, pulsars are born in the upper left part of the diagram, and evolve to longer periods and smaller period derivatives. It is not known on what timescale magnetic fields of pulsars decay. The lower right region represents a transition to pulsar death, when the emitted energy is too small to generate significant electron-positron pairs. The pulsars in the lower left corner are re-born, having been spun-up by accretion in binaries.

The actual emission is believed to be due to curvature radiation from electrons trapped in the magnetic field. Since the potential drop is of order 10^{15-16} V, electrons will have energies of about 10^{12} eV, and the photons produced will have energies many times $m_e c^2$. Thus additional electron-positron pairs will be produced and the resulting pair-cascade shorts out the electric field propelling the charges into space. The high density of electrons makes maser activity possible, which ultimately results in radio waves.

One major shortcoming of the magnetic dipole model concerns the braking index

$$n = -\frac{\Omega \ddot{\Omega}}{\dot{\Omega}^2}, \quad (1.4)$$

which implies a power-law deceleration with $\dot{\Omega} \propto -\Omega^n$. The dipole model predicts this to be 3, but observations of most pulsars yield a value significantly less than 3.

Shortly after the first pulsar was discovered, a pulsar was found to exist at the center of the Crab nebula, the expanding gaseous remnant of a supernova known to have been visible in 1054. Fig. 1.2 shows a stone painting of the supernova with the Moon. Comparing the observed expansion of the ejecta with their angular distances from the center of the nebula confirms the time of the explosion. The Crab pulsar strengthened the connection between neutron stars and some types of supernovae, those that are collectively known as gravitational collapse supernovae.

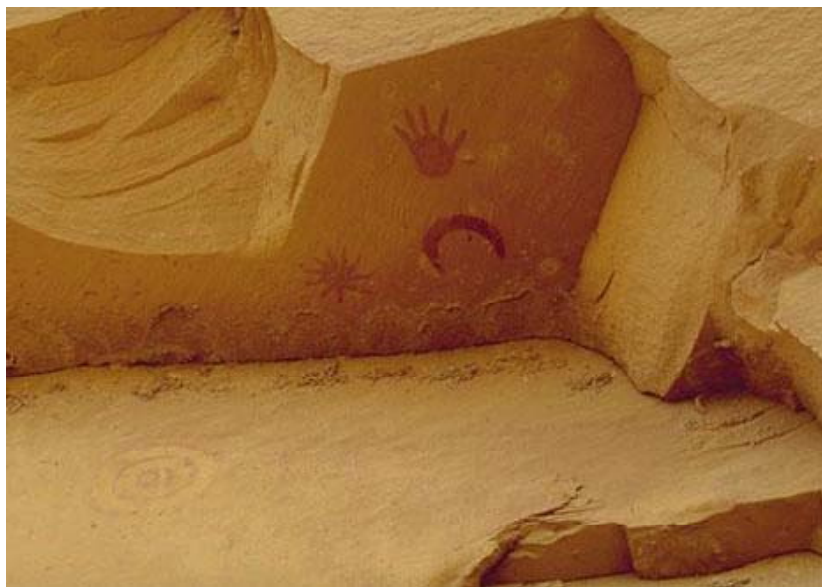


Figure 1.2: Anasazi rock painting showing SN 1054 and a crescent moon.

In 1975, Hulse and Taylor⁶ discovered a pulsar which was orbiting another star. Although this star has never been directly observed, its presence is deduced because of an additional periodicity imposed on the pulse stream. A straightforward application of Kepler's Law The Doppler shift of the pulses, together with the orbital period, revealed that the combined masses of the two stars was about $2.8 M_{\odot}$. The fact that no tidal distortions were apparently affecting the orbital motion, and the momentous discovery that the orbit was slowly shrinking, presumably due to the predicted emission of gravitational radiation, allowed the measurements of the individual masses in this system. The invisible companion's mass turned out to be nearly equal to the pulsar's mass, about $1.4 M_{\odot}$. Although in principle, it could be a normal star or even a white dwarf, these possibilities are ruled out by its very invisibility.

Finally, in 1987, the first supernova observed that year, in the close-by irregular galaxy known as the Large Magellanic Cloud, produced a brief neutrino pulse observed by at least two neutrino observatories, the IMB detector in the Morton Salt Mine near Cleveland, and the Kamiokande detector in the Japanese Alps. Models of supernovae predict that the aftermath of a gravitational collapse supernova will involve the formation of a proto-neutron star. Such a star is not only hot, with temperatures of nearly 10^{11} K, but is also lepton rich in comparison with a cold neutron star. The high concentration of leptons, which is the sum of the electron and neutrino concentrations, is mandated by the fact that neutrinos

are trapped within the proto-neutron star at least for many seconds after its formation. Neutrinos are formed during gravitational collapse due to electron capture reactions induced by the increasing electron chemical potential. The duration of the neutrino burst, the average energy of the neutrinos, and the total number of neutrinos observed were all in accord with theoretical predictions⁷.

A massive amount of energy is released in a gravitational collapse supernova. Compared to the binding energy of the massive star that forms its progenitor, the binding energy of a neutron star is huge, about $GM^2/R \sim 3 \times 10^{53}$ ergs for $M = 1.4 M_\odot$ and radius $R = 15$ km. The weak interaction cross section for neutrino scattering and absorption is $\sigma_0 \sim 4 \times 10^{-44} (E_\nu/\text{MeV})^2 \text{ cm}^2$, where E_ν is the neutrino energy. We estimate the mean neutrino energy as the Fermi energy of degenerate neutrinos

$$E_\nu = \hbar c (6\pi^2 \rho N_0 Y_\nu)^{1/3} \simeq 103 \rho_{14}^{1/3} Y_{\nu,0.04}^{1/3} \text{ MeV}, \quad (1.5)$$

where $Y_{\nu,0.04} = Y_\nu/0.04$ is the concentration of neutrinos in dense proto-neutron star matter scaled to 0.04, and ρ_{14} is the density scaled to $10^{14} \text{ g cm}^{-3}$. The typical neutrino mean free path is then about

$$\lambda \simeq \frac{1}{\rho N_0 \sigma_0} = 39.3 \rho_{14}^{-5/3} Y_{\nu,0.04}^{-2/3} \text{ cm}. \quad (1.6)$$

Compared to the core size of about

$$R \simeq \left(\frac{15M}{8\pi\rho} \right)^{1/3} \simeq 16.8 \left(\frac{M_{1M_\odot}}{\rho_{14}} \right)^{1/3} \text{ km},$$

this is very small (M_{1M_\odot} is the mass in units of solar masses). Diffusion of the neutrinos out of the core takes a time

$$t_{diff} \simeq \frac{3R^2}{c\lambda} = 7.2 \rho_{14} (M_{1M_\odot} Y_{\nu,0.04})^{1/3} \text{ s}.$$

As the neutrinos diffuse out of the core, they both lose energy and encounter matter of lower density. Eventually, they reach a surface of last-scattering, or neutrinosphere, and escape. The condition on optical depth

$$\tau = \int_{R-\Delta R}^R \frac{dr}{\lambda} \simeq 1,$$

leads to an estimate for the depth ΔR under the surface where the neutrinosphere lies. One finds to order unity that $\Delta R \simeq \sqrt{\lambda_0 R}$ where λ_0 is the central value of the mean free path. One can also see that the density at the neutrinosphere is approximately

$$\rho(R - \Delta R) \simeq 2\rho_0 \frac{\Delta R}{R} \simeq 2\rho_0 \sqrt{\frac{\lambda_0}{R}} \simeq 0.01 \rho_{14}^{1/3} Y_{\nu,0.04}^{-1/3} M_{1M_\odot}^{-1/6}. \quad (1.7)$$

Although neutrinos at the neutrinosphere are not degenerate, using the degenerate approximation Eq. (1.5) allows us to estimate their mean escaping energy, which is

$$E_{\nu,esc} \simeq 22 \rho_{14}^{1/9} Y_{\nu,0.04}^{2/9} M_{1M_\odot}^{-1/18} \text{ MeV}. \quad (1.8)$$

Thus, although the timescale for diffusion is proportional to the assumed central density, the energies of the escaping neutrinos are very insensitive to assumptions about the central density and mass of the proto-neutron star (and by inference to the details of the neutrino opacity). It is quite remarkable that the observations of neutrinos from SN 1987A were in accord with all aspects of the above discussion: total emitted energy, timescale and average neutrino energy.

2. The Equation of State

The equation of state refers to the equations describing how the pressure and other thermodynamic variables such as the free energy and entropy depend upon the quantities of density, temperature and composition. For high density matter, such as is found in neutron stars, the composition is not well understood. Even if it were, the equation of state would remain highly uncertain. This is in contrast to most other astrophysical objects, such as normal stars and white dwarfs, in which the equation of state can be (mostly) adequately described by that of a perfect (non-interacting) gas.

Nevertheless, the equation of state of a non-interacting fermion gas serves as a useful framework. The extension of the equation of state to the highly interacting case will also be discussed, using a phenomenological approach that can be considered as an extrapolation from the relatively well-understood matter found in atomic nuclei.

2.1. Equation of State of a Perfect Fermion Gas

The energy of a non-interacting particle is related to its rest mass m and momentum p by the relativistic relation

$$E^2 = m^2 c^4 + p^2 c^2. \quad (2.1)$$

The occupation index is the probability that a given momentum state will be occupied. For fermions, it is:

$$f = \left[1 + \exp \left(\frac{E - \mu}{T} \right) \right]^{-1}, \quad (2.2)$$

where μ is the chemical potential. When the particles are interacting, E generally contains an effective mass and an interaction energy contribution. μ corresponds to the energy change when a particle is added to or subtracted from the system. We will use units such that $k_B=1$; thus $T = 1$ MeV corresponds to $T = 1.16 \times 10^{10}$ K.

The number and internal energy densities are given, respectively, by

$$n = \frac{g}{h^3} \int f d^3 p; \quad \epsilon = \frac{g}{h^3} \int E f d^3 p \quad (2.3)$$

where g is the spin degeneracy ($g = 2j + 1$ for massive particles, where j is the spin of the particle, i.e., $g = 2$ for electrons, muons and nucleons, $g = 1$ for neutrinos). The entropy per baryon s can be expressed as

$$ns = -\frac{g}{h^3} \int [f \ln f + (1 - f) \ln (1 - f)] d^3 p \quad (2.4)$$

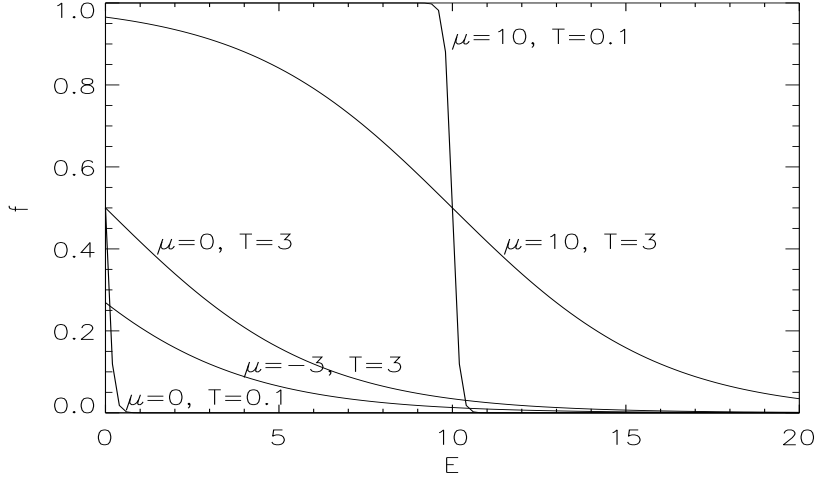


Figure 2.1: Occupation probabilities for various μ and T ; all energies are in MeV.

and the thermodynamic relations

$$P = n^2 \left. \frac{\partial(\epsilon/n)}{\partial n} \right|_s = Tsn + \mu n - \epsilon \quad (2.5)$$

gives the pressure. Incidentally, the two expressions (Eqs. (2.4) and (2.5)) are generally valid for interacting gases, also. We also note, for future reference, that

$$P = \frac{g}{3h^3} \int p \frac{\partial E}{\partial p} f d^3p. \quad (2.6)$$

Thermodynamics gives also that

$$n = \left. \frac{\partial P}{\partial \mu} \right|_T; \quad ns = \left. \frac{\partial P}{\partial T} \right|_\mu. \quad (2.7)$$

Note that if we define degeneracy parameters $\phi = \mu/T$ (useful in the relativistic case) and $\psi = (\mu - mc^2)/T$ (useful in the non-relativistic case) the following relations are valid:

$$P = -\epsilon + n \left. \frac{\partial \epsilon}{\partial n} \right|_T + T \left. \frac{\partial P}{\partial T} \right|_n; \quad \left. \frac{\partial P}{\partial T} \right|_\phi = ns + n\phi; \quad \left. \frac{\partial P}{\partial T} \right|_\psi = ns + n\psi. \quad (2.8)$$

In general, these equations are non-analytic except in limiting cases and full integrations are necessary. A useful two-dimensional polynomial expansion has been developed by Eggleton, Flannery and Faulkner⁸ and refined by Johns, Ellis and Lattimer⁹. Fig. 2.2 shows the behavior of various thermodynamic quantities in the density-temperature plane for an ideal gas.

In many situations, one or the other of the following limits may be realized: extremely degenerate ($\phi \rightarrow +\infty$), nondegenerate ($\phi \rightarrow -\infty$), extremely relativistic ($p \gg mc$), non-relativistic ($p \ll mc$). In particular, it is useful to examine the cases of extreme degeneracy and extreme relativity (EDER), extreme degeneracy and non-relativity (EDNR), and non-degeneracy and non-relativity (NDNR).

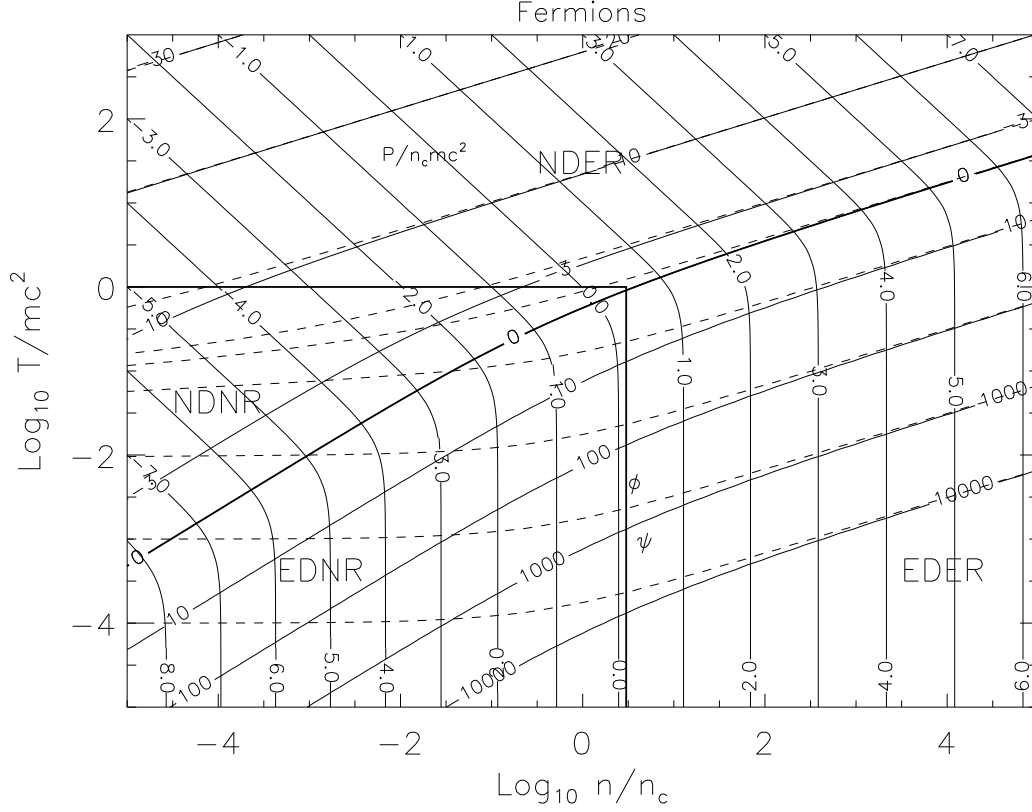


Figure 2.2: Thermodynamics of a perfect fermion gas. Contours of ψ (solid curves) and ϕ (dashed curves) run from lower left to upper right. Orthogonal solid lines show contours of $\log_{10} P/(n_c mc^2)$, where $n_c = (g/2\pi^2)(mc/\hbar)^3$. The four regions where limiting approximations are valid, i.e., extreme cases of degeneracy and relativity, are indicated by NDNR, EDNR, EDER and NDER, respectively. These regions are separated by the curves $\psi = 0$ and the lines $T = mc^2$ and $n = 3n_c$.

2.1.1. Extreme degeneracy and relativity

In this case, the rest mass is negligible. The pressure is proportional to $n^{4/3}$.

$$\begin{aligned}
 n &= \frac{g}{6\pi^2} \left(\frac{\mu}{\hbar c} \right)^3 \left[1 + \left(\frac{\pi}{\phi} \right)^2 + \dots \right], \\
 \frac{\epsilon}{3} = P &= \frac{n\mu}{4} \left[1 + \left(\frac{\pi}{\phi} \right)^2 + \dots \right], & \mathbf{EDER} & \quad (2.9) \\
 s &= \pi^2/\phi + \dots
 \end{aligned}$$

2.1.2. Extreme degeneracy and non-relativity

The pressure is proportional to $n^{5/3}$.

$$\begin{aligned} n &= \frac{g}{6\pi^2} \left(\frac{2m\psi T}{\hbar^2} \right)^{3/2} \left[1 + \frac{1}{8} \left(\frac{\pi}{\psi} \right)^2 + \dots \right], \\ \frac{2}{3} (\epsilon - nmc^2) &= P = \frac{2n\psi T}{5} \left[1 + \frac{1}{2} \left(\frac{\pi}{\psi} \right)^2 + \dots \right], \\ s &= \pi^2/2\psi + \dots. \end{aligned} \quad \text{EDNR} \quad (2.10)$$

2.1.3. Non-degeneracy and non-relativity

$$\begin{aligned} n &= g \left(\frac{mT}{2\pi\hbar^2} \right)^{3/2} e^{\psi}, \\ 2(\epsilon - nmc^2)/3 &= P = nT, \\ s &= 5/2 - \psi. \end{aligned} \quad \text{NDNR} \quad (2.11)$$

2.1.4. Relativistic including particle-antiparticle pairs

In chemical equilibrium, the chemical potential of antiparticles $\mu^{(-)} = -\mu^{(+)}$, where $\mu = \mu^{(+)}$ is the chemical potential of the particles. This situation is appropriate for trapped neutrinos, and also for electrons above 10^6 g cm^{-3} or $T > 0.5 \text{ MeV}$.

$$\begin{aligned} n &= n^{(+)} - n^{(-)} = \frac{g}{6\pi^2} \left(\frac{T}{\hbar c} \right)^3 \left[1 + \left(\frac{\pi T}{\mu} \right)^2 \right], \\ \frac{\epsilon}{3} &= P = \frac{g\mu}{24\pi^2} \left(\frac{\mu}{\hbar c} \right)^3 \left[1 + 2 \left(\frac{\pi T}{\mu} \right)^2 + \frac{7}{15} \left(\frac{\pi T}{\mu} \right)^4 \right], \\ s &= \frac{gT\mu^2}{6n(\hbar c)^2} \left[1 + \frac{7}{15} \left(\frac{\pi T}{\mu} \right)^2 \right]. \end{aligned} \quad (2.12)$$

Note that the equation for the density can be inverted to yield

$$\mu = r - q/r, \quad r = \left[(q^2 + r^2)^{1/2} + t \right]^{1/3}, \quad t = \frac{3\pi^2}{g} n (\hbar c)^3, \quad q = \frac{(\pi T)^2}{3}. \quad (2.13)$$

2.2. Interacting Fermi Gas

Most equations of state for neutron stars are based on one of two approaches – non-relativistic potential models or relativistic field-theoretical models. Examples of the former include Skyrme forces, while Walecka-type models are examples of the latter. We present only a brief descriptions of non-relativistic models¹⁰.

2.2.1. Non-relativistic potential models

The uniform matter energy density, which is dependent upon particle densities and temperature only, is given by a bulk Hamiltonian density H_B

$$\epsilon(n_n, n_p, T) = H_B(n_n, n_p, \tau_n, \tau_p), \quad (2.14)$$

which is a functional of both nucleon densities (n_n, n_p) and the auxiliary variables of kinetic energy densities (τ_n, τ_p) . Treating the single particle states as plane waves, the so-called Thomas-Fermi approximation, the single particle energies of the nucleons are defined by

$$E_t(p) = \frac{\partial H_B}{\partial \tau_t} p^2 + \frac{\partial H_B}{\partial n_t} \equiv \frac{\hbar^2}{2m_t^*} p^2 + V_t. \quad (2.15)$$

It is convenient to have thereby defined the effective nucleon masses m_t^* and interaction potentials V_t . $t = n, p$ is the isospin index. The occupation probabilities are

$$f_t(p, T) = [\exp([\epsilon_t(p) - \mu_t]/T) + 1]^{-1}, \quad (2.16)$$

The number and kinetic densities become

$$n_t = (2\pi^3 \hbar^3)^{-1} \int_0^\infty f_t(p, T) d^3 p = \frac{1}{2\pi^2 \hbar^3} \left(\frac{2m_t^* T}{\hbar^2} \right)^{3/2} F_{1/2}(\eta_t), \quad (2.17a)$$

$$\tau_t = (2\pi^3 \hbar^5)^{-1} \int_0^\infty f_t(p, T) p^2 d^3 p = \frac{1}{2\pi^2 \hbar^5} \left(\frac{2m_t^* T}{\hbar^2} \right)^{5/2} F_{3/2}(\eta_t), \quad (2.17b)$$

where F_i is the normal Fermi integral

$$F_i(\eta) = \int_0^\infty \frac{u^i}{1 + \exp(u - \eta)} du, \quad (2.18)$$

and $\eta_t = (\mu_t - V_t)/T$ is the degeneracy parameter. It is also clear that the uniform matter energy density can be written now as a sum of kinetic and potential contributions

$$\epsilon = H_B = \sum_t \frac{\hbar^2}{2m_t^*(n_n, n_p)} \tau_t + U(n_n, n_p) \quad (2.19)$$

where U is the potential energy density. Therefore, the bulk nuclear force is completely specified by the *density* dependance of m^* and U . The temperature contributions enter only from the Fermi statistics in the kinetic energy term.

From Eq. (2.15) it can be seen that V_t satisfies

$$V_t = \frac{\hbar^2}{2} \sum_s \tau_s \frac{\partial (m_s^*)^{-1}}{\partial n_t} + \frac{\partial U}{\partial n_t}. \quad (2.20)$$

The entropy density of interacting Fermi-Dirac particles is

$$S_t = \frac{1}{2\pi^3 \hbar^2} \int_0^\infty f_t \ln f_t + (1 - f_t) \ln (1 - f_t) d^3 p = \frac{5\hbar^2 \tau_t}{6m_t^* T} - n_t \eta_t. \quad (2.21)$$

The pressure is

$$P = \sum_t (n_t \mu_t + T S_t) - E = \sum_t \left(n_t V_t + \frac{\hbar^2 \tau_t}{3m_t^*} \right) - U. \quad (2.22)$$

The free energy density F is

$$F = \epsilon - TS = \sum_t \left(n_t \eta_t - \frac{\hbar^2 \tau_t}{3m_t^*} \right) + U. \quad (2.23)$$

2.2.2. Schematic Hamiltonian density

Models for the Hamiltonian density can be relatively complicated, but many of the concepts can be illustrated by using a parametrized energy density

$$\epsilon(n, T, x) = n \left[B + \frac{K}{18} \left(1 - \frac{n}{n_0} \right)^2 + S_v \frac{n}{n_0} (1 - 2x)^2 + a \left(\frac{n_0}{n} \right)^{2/3} T^2 \right]. \quad (2.24)$$

Actually, this is an excellent approximation in the vicinity of the nuclear saturation density $n \sim n_0 \simeq 0.16 \text{ fm}^{-3}$ (corresponding to a mass density of about $\rho_{14} = 2.7$ for cold ($T = 0$), symmetric ($x = 1.2$) matter. In Eq. (2.24), $B \simeq -16 \text{ MeV}$ represents the binding energy of cold symmetric matter at the saturation density, $K \simeq 225 \text{ MeV}$ is the incompressibility parameter, $S_v \simeq 30 \text{ MeV}$ is the volume symmetry energy parameter, and $a \simeq (15 \text{ MeV})^{-1}$ is the nuclear level density parameter. In other words, Eq. (2.24) represents an three-dimensional expansion for the energy in the vicinity of $n = n_0, T = 0$ and $x = 1/2$. However, we will utilize this energy function with some success even under extreme extrapolations, such as to very low and high densities, to moderate temperatures, and to extremely neutron-rich matter. Even though this model appear to break down in some circumstances, in almost all situations its use remains justifiable. For example, the energy per baryon is finite at zero density and temperature unless $B = -K/18$, and is infinite at zero density and finite temperatures. Nevertheless, in most applications we need the energy density rather than the specific energy, and this of course vanishes at zero density.

Two of the parameters in Eq. (2.24), B and S_v , are constrained by nuclear masses and K has been constrained by giant monopole resonances in nuclei. The level density

parameter is also constrained by laboratory measurements. However, these constraints are not perfect because nuclei have finite size while Eq. (2.24) refers to infinite matter. Therefore surface and Coulomb effects have to be considered. Because surface effects are generally reduced compared to volume effects by a factor $A^{-1/3}$, they remain large even in the largest nuclei. For example, it is believed that surface contributions to the nuclear specific heat (i.e., the a parameter) are fully equal to the volume contribution. In a similar way, surface energies, surface symmetry energies and incompressibility contributions are comparable to volume terms and difficult to uniquely determine.

From the energy density of uniform matter Eq. (2.24), one can determine the pressure, chemical potentials and entropy density:

$$\begin{aligned}
 P &= \frac{n^2}{n_0} \left[\frac{K}{9} \left(\frac{n}{n_0} - 1 \right) + S_v (1 - 2x)^2 \right] - \frac{2a}{3} n \left(\frac{n_0}{n} \right)^{2/3} T^2, \\
 \mu_n &= B + \frac{K}{18} \left(1 - \frac{n}{n_0} \right) \left(1 - 3 \frac{n}{n_0} \right) + 2S_v \frac{n}{n_0} (1 - 4x^2) - \frac{a}{3} \left(\frac{n_0}{n} \right)^{2/3} T^2, \\
 \hat{\mu} &= 4S_v \frac{n}{n_0} (1 - 2x), \\
 S &= 2an \left(\frac{n_0}{n} \right)^{2/3} T.
 \end{aligned} \tag{2.25}$$

These approximations have a number of believable aspects: the pressure vanishes both at zero density and at n_0 , and is negative in-between, and the neutron and proton chemical potentials tend to negative infinity in the limit of low density. The latter is the correct behavior, valid for a non-degenerate gas, even though Eq. (2.24) is a degenerate expansion.

2.3. Phase Coexistence

We saw that the pressure, at zero temperature, in the density range from 0 to n_0 is negative. Ordinary matter cannot exist in such a condition. In practice, matter will separate into two phases, both with the same pressure, in this case 0. We can illustrate that dividing such matter into two phases with different densities will result in a lower free energy than a single uniform phase at the same average density. Plus, the pressure of the two-phase mixture will no longer be negative.

Matter in the two phases in phase coexistence will have to be in chemical and pressure equilibrium. This can be illustrated simply for the case of symmetric matter. The total free energy density of this system will satisfy

$$F_1 = uF_I + (1 - u) F_{II}, \tag{2.26}$$

$$n = un_I + (1 - u) n_{II}. \tag{2.27}$$

Minimizing F_1 with respect to n_I and u , using the density constraint to eliminate n_{II} , results in

$$\begin{aligned}
 \frac{\partial F_1}{\partial n_I} &= u \frac{\partial F_I}{\partial n_I} + (1 - u) \frac{\partial F_{II}}{\partial n_{II}} \left(\frac{-u}{1 - u} \right) = 0, \\
 \frac{\partial F_1}{\partial u} &= F_I - F_{II} + (1 - u) \frac{\partial F_{II}}{\partial n_{II}} \left(\frac{-n_I}{1 - u} + \frac{n_{II}}{1 - u} \right) = 0.
 \end{aligned} \tag{2.28}$$

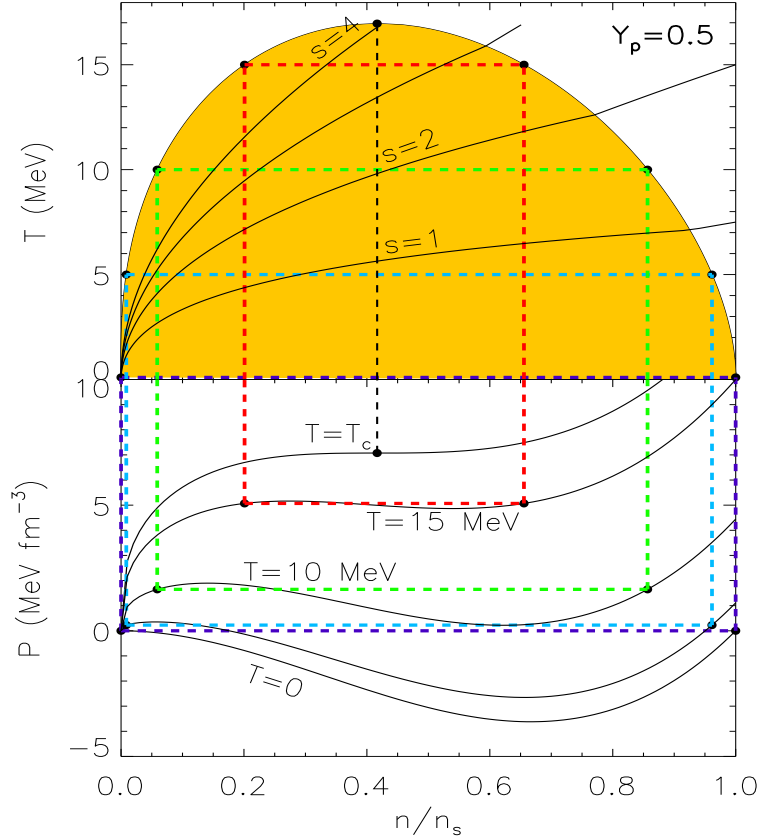


Figure 2.3: Lower panel: Pressure isotherms for the schematic energy density for $x = 1/2$. Dashed lines connect the two densities satisfying equilibrium conditions. Upper panel: The coexistence region in the density-temperature plane is colored yellow. The critical density and temperature are indicated by a filled black circle. Entropy per baryon contours are also displayed. Parameters used were $K = 225 \text{ MeV}$, $a = (15 \text{ MeV})^{-1}$.

These result in the equilibrium conditions

$$\mu_I = \mu_{II}, \quad P_I = P_{II},$$

where $\mu = \partial F/\partial n$. Approximately, for the schematic energy density Eq. (2.24) in the limit $T \rightarrow 0$, these equations have the solution $n_I = n_0$ and $n_{II} \approx 0$. In this case $P_I = P_{II} = 0$ and $\mu_I = \mu_{II} \simeq B$. (Note that one has to work in the limit $T \rightarrow 0$ rather than use $T = 0$.) Since $u = n/n_s$, one finds that $F_1 = nB$.

On the other hand, uniform matter at the density n will have a free energy density

$$F_2 = n \left[B + \frac{K}{18} \left(1 - \frac{n}{n_0} \right)^2 \right] = F_1 + n \frac{K}{18} \left(1 - \frac{n}{n_0} \right)^2.$$

Obviously, $F_2 > F_1$. System 1 is preferred, and has a physically achievable pressure, unlike system 2 for which $P_2 < 0$.

At finite temperature, phase coexistence is still possible, but for a lessened density range. Fig. 2.3 shows the phase coexistence region for the parametrized energy density

of Eq. (2.24). The lower part of the figure displays the pressure along isotherms, and the dashed lines connect the densities where the equilibrium conditions are satisfied. It is clear that a maximum temperature exists for which two-phase equilibrium is possible. This critical temperature T_c , and the accompanying critical density n_c , is defined by the conditions

$$\frac{\partial P}{\partial n} = \frac{\partial^2 P}{\partial n^2} = 0.$$

For the energy density of Eq. (2.24), one can show that

$$n_c = \frac{5}{12}n_0, \quad T_c = \left(\frac{5}{12}\right)^{1/3} \left(\frac{5K}{32a}\right)^{1/2}, \quad s_c = \left(\frac{12}{5}\right)^{1/3} \left(\frac{5Ka}{8}\right)^{1/2},$$

where s_c is the entropy per baryon at the critical point.

When matter is asymmetric, that is $Y_e < 1/2$, an additional constraint corresponding to charge neutrality is enforced:

$$nY_e = un_I x_I + (1-u)n_{II} x_{II}, \quad (2.29)$$

where Y_e is the ratio of protons to baryons (the number of electrons equals the number of protons for charge neutrality). Minimizing the free energy density Eq. (2.26) using Eqs. (2.29) and (2.27) results in the equilibrium conditions

$$\mu_{n,I} = \mu_{n,II}, \quad \mu_{p,I} = \mu_{p,II}, \quad P_I = P_{II}. \quad (2.30)$$

While the resulting phase coexistence region remains similar to that found in Fig. 2.3, the maximum temperature for coexistence is less than T_c and the pressure along isotherms steadily increases through the two-phase region rather than remaining constant.

2.4. Nuclear Droplet Model

The results for phase coexistence illustrate that at zero temperature, the entire region with densities less than n_0 consists of nuclei: the dense phase within nuclei is in equilibrium with the surrounding gas. The density inside nuclei is close to the saturation density n_0 . However, the phase coexistence model only demonstrates that matter divides into two phases, but does not indicate the sizes of the resulting nuclei. To a very good approximation, finite-size effects of nuclei can be described by a droplet model. This approach was considered for zero temperature nuclei in dense matter originally by Baym, Bethe and Pethick¹¹. Lattimer et al.¹² extended the treatment to finite temperature, corrected the treatment of the surface energy, and introduced the concept of using consistent nuclear interactions for matter both inside and outside the nuclei. Lattimer and Swesty¹³ extended the treatment to include nuclear shape variations and alternate nuclear interactions. The treatment described here is based on Ref. 12 and Ref. 13, and further details can be sought therein. Essentially, Eq. (2.26) is modified:

$$F_1 = u \left(F_I + \frac{f_{LD}}{V_N} \right) + (1-u) F_{II}, \quad (2.31)$$

where the liquid droplet energy of a nucleus is $f_{LD} = f_S + f_C + f_T$, where the three major finite-size effects concern surface, Coulomb and translational contributions, respectively. To leading order, these effects can be considered separately.

2.4.1. Nuclear Coulomb energy

The Coulomb energy of a uniform density charged sphere is $3(Ze)^2/(5R_N)$, where R_N is the nuclear radius. As calculated in Ref. 11, at high densities this energy is modified by the close proximity of other nuclei (lattice effects). In the Wigner-Seitz approximation, the uniform density nucleus is contained within a neutral sphere of volume $V_c = V_N/u$, where $V_N = 4\pi R_N^3/3$ is the nuclear volume. The background neutralizing electrons are uniformly distributed within V_c . Finite temperature effects may be ignored. The total Coulomb free energy of this configuration is

$$f_c = \frac{3}{5} \frac{Z^2 e^2}{R_N} \left(1 - \frac{3}{2} u^{1/3} + \frac{u}{2} \right) \equiv \frac{3}{5} \frac{Z^2 e^2}{R_N} D(u). \quad (2.32)$$

The function D used here is for spherical nuclei. However, as Ravenhall, Pethick and Wilson¹⁴ showed, nuclear deformations and changes to rods or plates can be accommodated by a suitable modification of D . For more discussion, see Ref. 13, and also see Fig. 3.1.

2.4.2. Nuclear translational energy

Nuclei themselves are (relatively) non-interacting, non-degenerate and non-relativistic. Hence, in addition to their internal energies, they have a translational free energy per nucleus of

$$f_T = T \ln \left(\frac{u}{n_Q V_N A^{3/2}} \right) - T \equiv \mu_T - T, \quad n_Q = \left(\frac{m_b T}{2\pi \hbar^2} \right)^{3/2}. \quad (2.33)$$

To simplify the following algebra, we choose to modify this result to

$$f_T = \frac{V_N n_I}{A_0} (\mu_T - T) \equiv \frac{V_N n_I}{A_0} \left[\ln \left(\frac{u n_I}{n_Q A_0^{5/2}} \right) - 1 \right], \quad (2.34)$$

where $A_0 \simeq 60$ is taken to be a constant.

2.4.3. Nuclear surface energy

In principle, one can consider the surface energy of a sphere to be the area multiplied by the surface tension. However, in terms of thermodynamics, the surface tension is actually a surface thermodynamic potential density. In any case, the surface tension can be calculated by minimizing the total free energy involved in a semi-infinite interface. The minimization is a functional variation because the free energy must be optimized with respect to the density profile across the interface. Up until now, we have considered only the volume free energy of uniform nuclear matter. But in the vicinity of the nuclear surface, the density is rapidly varying. This introduces an additional gradient term to the total free energy density, which to lowest order can be written

$$F = F_I + F_\nabla = F_I(n) + \frac{1}{2} Q(n) (\nabla n)^2, \quad (2.35)$$

where $F_I(n)$ is the uniform matter energy density and $F_{\nabla}(n, \nabla n)$ contain gradient contributions.

First, consider symmetric matter so only one species of nucleon need be included. We need to minimize the total free energy subject to the constraint of a fixed number of particles

$$\tilde{f} = \int_0^{\infty} (F - \mu n) d^3r \simeq 4\pi R_N^2 \int_{-\infty}^{\infty} (F - \mu n) dx \quad (2.36)$$

where F is the free energy density and μ is a Lagrange parameter that turns out to be the chemical potential of the system. The right-hand side of this expression represents the leptodermous expansion to a semi-infinite interface. Note that $F - \mu n$ vanishes at large distances from the surface so that the integral is finite. As $x \rightarrow +\infty$ this result is trivial, since both F and n vanish. As $x \rightarrow -\infty$ this requires that $\mu = F(n_0)/n_0$, where in the symmetric matter case n_0 is the saturation density. In this model, the surface radius is defined by

$$\int_0^{\infty} n d^3r = 4\pi n_0 R_N^3 / 3 = A.$$

Also note that since μA is the energy of A nucleons at the saturation density that the nuclear surface energy is just $f_S \equiv f_{min}$, the minimized energy in Eq. (2.36).

To proceed, we assume for simplicity that Q is independent of density, although this is not necessary. Minimizing Eq. (2.36), which is equivalent to minimizing the argument of the integral only, we find

$$\frac{\partial F_I}{\partial n} - \mu - Qn'' = 0. \quad (2.37)$$

Derivatives with respect to density are indicated by $'$'s. Multiplying this equation by n' , it can be integrated to yield

$$\frac{1}{2} Q n'^2 = F_I - \mu n. \quad (2.38)$$

We chose the constant of integration to ensure that the density gradient vanishes far from the interface. This equation can be further integrated to yield the density profile, although this step is not necessary to determine the surface tension. Substituing Eq. (2.38) into Eq. (2.36) thus gives

$$\begin{aligned} \sigma &= \int_{-\infty}^{\infty} (F - \mu n) dx = \int_{-\infty}^{\infty} \left(F_I - \mu n + \frac{Q}{2} n'' \right) dx = 2 \int_{-\infty}^{\infty} (F_I - \mu n) dx \\ &= \sqrt{2Q} \int_0^{n_0} \sqrt{F_I - \mu n} dn. \end{aligned} \quad (2.39)$$

As an example, consider the schematic free energy density Eq. (2.24) in the case of symmetric matter and zero temperature. We have $\mu = B$. The surface energy becomes, using Eq. (2.39),

$$\sigma = \frac{1}{3} \sqrt{QKn_0^3} \int_0^{n_0} \left(\frac{n}{n_0} \right)^{1/2} \left(1 - \frac{n}{n_0} \right) d \left(\frac{n}{n_0} \right) = \frac{4}{45} \sqrt{QKn_0^3}. \quad (2.40)$$

In this case there is no difference between the surface free energy per unit area and the surface tension, or thermodynamic potential per unit area, because the pressure at both boundaries vanishes. The surface free energy is thus $4\pi R_N^2 \sigma$.

For asymmetric matter, we choose $x_0 = n_{p\infty}/n_\infty$ to be the proton fraction in the dense phase. There are two constraints, one each for proton number and neutron number. In this case

$$\sigma = \int_{-\infty}^{\infty} (F - \mu_n n_n - \mu_p n_p - P_\infty) dx, \quad (2.41)$$

where

$$F = F_I + \frac{1}{2} \left[Q_{nn} (\nabla n_n)^2 + 2Q_{np} \nabla n_n \nabla n_p + Q_{pp} (\nabla n_p)^2 \right]. \quad (2.42)$$

Also, P_∞ is the equilibrium pressure. Minimizing the integrand of Eq. (2.41) with respect to the neutron and proton density profiles, one finds

$$\begin{aligned} Q_{nn} n_n'' + Q_{np} n_p'' &= \frac{\partial F_I}{\partial n_n} - \mu_n, \\ Q_{np} n_n'' + Q_{pp} n_p'' &= \frac{\partial F_I}{\partial n_p} - \mu_p. \end{aligned} \quad (2.43)$$

These can be written as

$$\begin{aligned} (Q_{nn} + Q_{np}) n'' &= \frac{\partial F_I}{\partial n_n} - \mu_n + \frac{\partial F_I}{\partial n_p} - \mu_p = 2 \frac{\partial F_I}{\partial n} - \mu_n - \mu_p, \\ (Q_{nn} - Q_{np}) \alpha'' &= \frac{\partial F_I}{\partial n_n} - \mu_n - \frac{\partial F_I}{\partial n_p} + \mu_p = 2 \frac{\partial F_I}{\partial \alpha} - \hat{\mu}. \end{aligned} \quad (2.44)$$

We introduced the asymmetry density as $\alpha = n_n - n_p$.

For the case of the schematic energy density at zero temperature, Eq. (2.24), P_∞ will vanish unless the proton fraction in the dense phase is so small that the neutron chemical potential there becomes positive. Assuming $P_\infty = 0$, one has

$$\begin{aligned} (Q_{nn} + Q_{np}) n'' &= \frac{K}{9} \left(3 \frac{n - n_\infty}{n_0} - 4 \right), \\ (Q_{nn} - Q_{np}) \alpha'' &= \frac{4S_v}{n_0} (\alpha - \alpha_\infty), \end{aligned} \quad (2.45)$$

where $\alpha_\infty = n_\infty(1 - 2x_\infty)$. We introduced the equilibrium density n_∞ in the dense phase, defined by

$$\frac{n_\infty}{n_0} = 1 - \frac{9S_v}{K} (1 - 2x_\infty)^2. \quad (2.46)$$

Of course, for $x_\infty = 1/2$, $n_\infty = n_0$. Each of Eq. (2.36) can be integrated:

$$\begin{aligned} \frac{(Q_{nn} + Q_{np})}{2} n'^2 &= \frac{K}{9} \left(\frac{n_\infty - n}{n_0} \right)^2 (n + 2n_\infty - 2n_0), \\ \frac{Q_{nn} - Q_{np}}{2} \alpha'^2 &= \frac{2S_v}{n_0} (\alpha_\infty - \alpha)^2. \end{aligned} \quad (2.47)$$

It is apparent that the quantity σ is not a free energy but rather a thermodynamic potential density per unit area. A thermodynamic potential is a perfect differential of the chemical potential and the temperature. Thus we choose to write the surface tension as

$\sigma(\mu_s)$ where μ_s is the chemical potential of the nucleons in the surface¹⁵. The number of particles associated with the surface per unit area is $\nu_s = -\partial\sigma/\partial\mu_s$ from thermodynamics, and the surface free energy density is then $\sigma + \mu_s\nu_s$. Thus, if the surface tension is expressed as a quadratic expansion, and $P_\infty = 0$, one has

$$\sigma = \sigma_0 - \sigma_\delta(1 - 2x_I)^2, \quad \hat{\mu}_{II} = 4S_v(1 - 2x_I)n_\infty/n_0, \quad . \quad (2.48)$$

The determination of the function $\sigma(\mu_s)$ is discussed below.

2.4.4. Electron energy

Electrons form a nearly ideal and uniform gas, so the perfect fermion EOS discussed earlier is appropriate for them. The electron EOS does not affect the relative energies of the baryons, except for influencing the composition of matter in beta equilibrium. For the calculations described below, we employed the relations of Eq. (2.12).

2.4.5. Liquid droplet equilibrium conditions

The total nucleonic free energy density of matter containing nuclei in the droplet model can now be written:

$$\begin{aligned} F_1 &= uF_I + (1 - u)F_{II} + u\frac{4\pi R_N^2}{V_N}(\sigma + \mu_s\nu_s) + \frac{3}{5}\frac{Z^2e^2}{R_NV_N}D + \frac{un_I}{A_0}(\mu_T - T) \\ &= u\left[F_I + \frac{3}{R_N}(\sigma + \mu_s\nu_s) + \frac{4\pi}{5}(n_Ix_IeR_N)^2 + \frac{n_I}{A_0}(\mu_T - T)\right] + (1 - u)F_{II}. \end{aligned} \quad (2.49)$$

In addition, we have the conservation equations

$$n + un_I + (1 - u)n_{II}, \quad nY_e = un_Ix_I + (1 - u)n_{II}x_{II} + \frac{3u}{R_N}\nu_s. \quad (2.50)$$

Using these two equations to relate n_{II} and x_{II} to other variables, we minimize F_1 :

$$\begin{aligned} 0 &= \frac{1}{u}\frac{\partial F_1}{\partial n_I} = \mu_{n,I} - x_I\hat{\mu}_I - \mu_{n,II} + x_{II}\hat{\mu}_{II} + \hat{\mu}_{II}(x_I - x_{II}) \\ &\quad + \frac{8\pi}{5}n_I(x_IeR_N)^2D + \frac{\mu_T}{A_0}, \end{aligned} \quad (2.51a)$$

$$0 = \frac{\partial F_1}{\partial x_I} = un_I\left(\hat{\mu}_{II} - \hat{\mu}_I + \frac{8\pi}{5}x_I n_I(eR_N)^2D\right), \quad (2.51b)$$

$$0 = \frac{\partial F_1}{\partial \nu_s} = \frac{3u}{R_N}(\hat{\mu}_{II} + \mu_s), \quad (2.51c)$$

$$\frac{\partial F_1}{\partial \mu_s} = \frac{3u}{R_N}\left(\frac{\partial \sigma}{\partial \mu_s} + \nu_s\right), \quad (2.51d)$$

$$\begin{aligned} 0 &= \frac{\partial F_1}{\partial u} = F_I - F_{II} + \frac{3}{R_N}(\sigma + \mu_s\nu_s) + \frac{n_I}{A_0}\mu_T + (\mu_{n,II} - x_{II}\hat{\mu}_{II})(n_{II} - n_I) \\ &\quad + \frac{3}{R_N}\hat{\mu}_{II}\nu_s - n_I(x_I - x_{II}) + \frac{4\pi}{5}(n_Ix_IeR_N)^2(D + uD'), \end{aligned} \quad (2.51e)$$

$$0 = \frac{\partial F_1}{\partial R_N} = u\left[-\frac{3}{R_N^2}(\sigma + \mu_s\nu_s) + \frac{8\pi}{5}(n_Ix_Ie)^2R_N - \frac{3}{R_N^2}\hat{\mu}_{II}\nu_s\right]. \quad (2.51f)$$

These can be more compactly written as

$$\mu_{n,II} = \mu_{n,I} + \frac{\mu_T}{A_0}, \quad (2.52a)$$

$$\hat{\mu}_{II} = -\mu_s = \hat{\mu}_I + \frac{3\sigma}{R_N n_I x_I}, \quad (2.52b)$$

$$\nu_s = -\frac{\partial\sigma}{\partial\mu_s} = -\frac{\partial\sigma}{\partial x_I} \left(\frac{\partial\mu_s}{\partial x_I} \right)^{-1}, \quad (2.52c)$$

$$P_{II} = P_I + \frac{3}{2} \frac{\sigma}{R_N} \left(1 + \frac{u D'}{D} \right), \quad (2.52d)$$

$$R_N = \left(\frac{15\sigma}{8\pi n_I^2 x_I^2 e^2 D} \right)^{1/3}. \quad (2.52e)$$

These have simple physical interpretations: neutron and proton chemical equalities, modified by translation and Coulomb effects; pressure equality, modified by surface and Coulomb effects, the definition of the nucleon surface density, and, lastly, the Nuclear Virial Theorem, due to Baym, Bethe and Pethick, which states that the optimum nuclear size, for a given charge ratio, is set when the surface energy equals twice the Coulomb energy. We see that this theorem is correct only if the surface “energy” actually refers to the surface thermodynamic potential.

The overall pressure and chemical potentials of matter with nuclei can be simply stated:

$$P = P_{II} + P_e, \quad \mu_n = \mu_{n,II}, \quad \hat{\mu} = \hat{\mu}_{II}. \quad (2.53)$$

Some results of the liquid droplet EOS are displayed in Fig. 2.4 and Fig. 2.5, for $Y_e = 0.35$ and $Y_e = 0.02$, respectively. The electron contributions to all thermodynamics have been included. Also, photon contributions are also included. Note that nuclei persist to high temperatures even for very neutron-rich matter, although the mass fractions of nuclei in the most extreme case are only a few percent even at the lowest temperatures.

3. Internal Composition of Neutron Stars

A schematic view of the insides of a neutron star, courtesy of D. Page, is shown in Fig. 3.1. A neutron star can be considered as having five major regions, the inner and outer cores, the crust, the envelope and the atmosphere. The atmosphere and envelope contain a negligible amount of mass, but the atmosphere plays an important role in shaping the emergent photon spectrum, and the envelope crucially influences the transport and release of thermal energy from the star’s surface. The crust, extending approximately 1 to 2 km below the surface, primarily contains nuclei. The dominant nuclei in the crust vary with density, and range from ^{56}Fe for matter with densities less than about 10^6 g cm^{-3} to nuclei with $A \sim 200$ but $x \sim (0.1 - 0.2)$ near the core-crust interface at $n \approx n_0/3$. Such extremely neutron-rich nuclei are not observed in the laboratory, but rare-isotope accelerators hope to create some of them.

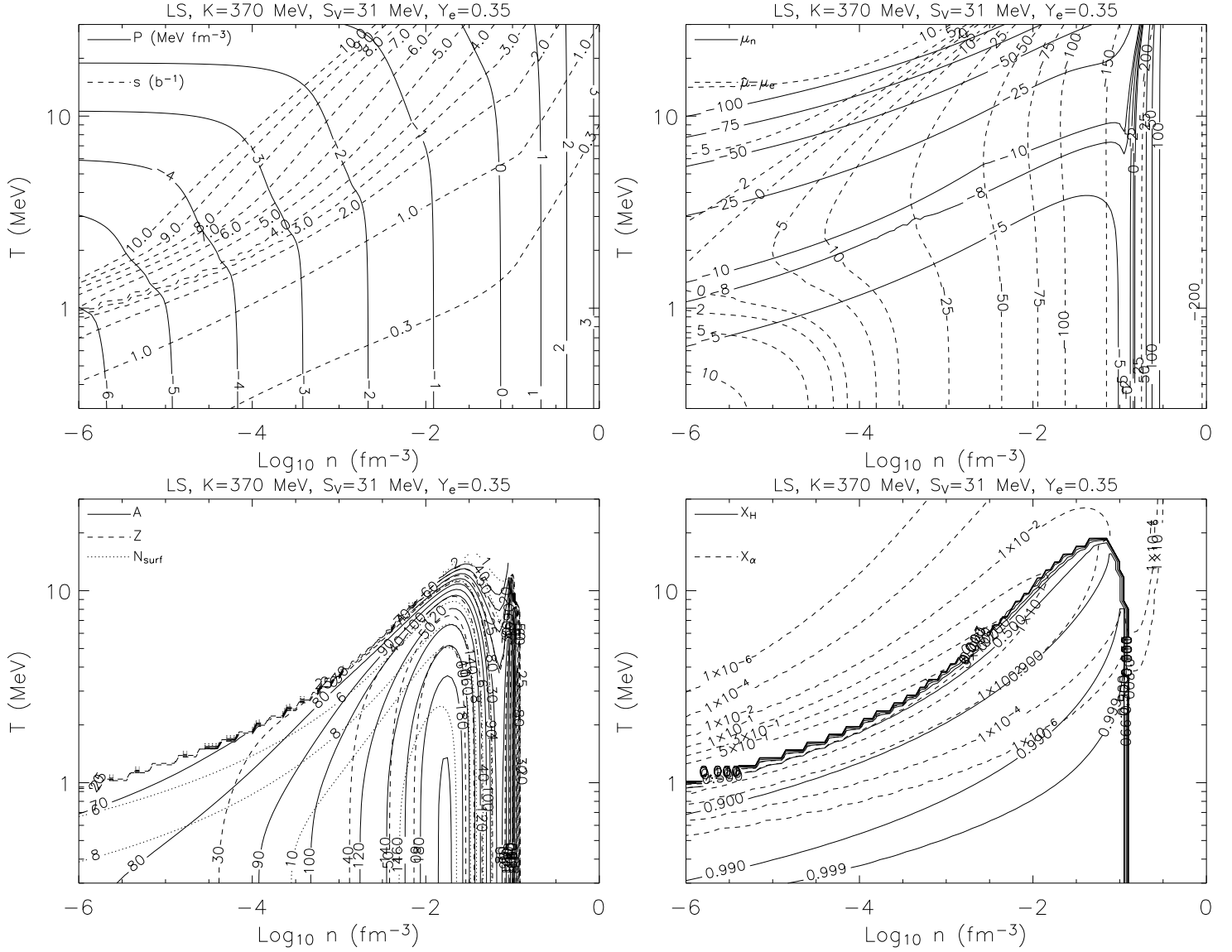


Figure 2.4: Liquid droplet EOS, parameters from Ref. 13. $Y_e = 0.35$
 Upperleft: Pressure and entropy contours. Upper right: Contours of μ_n
 and $\hat{\mu} - \mu_e$. Lower left: A, Z and $N_s = 4\pi R_N^2 \nu_s$ contours. Lower right:
 Contours of mass fractions of heavy nuclei (X_H) and α particles (X_α).

Within the crust, at densities above the so-called “neutron drip” density $4 \times 10^{11} \text{ g cm}^{-3}$ where the neutron chemical potential (the energy required to remove a neutron from the filled sea of degenerate fermions) is zero, neutrons leak out of nuclei. At the highest densities in the crust, more of the matter resides in the neutron fluid than in nuclei. At the core-crust interface, nuclei are so closely packed that they are virtually touching. It could well be that at somewhat lower densities, the nuclear lattice turns “inside-out” and forms a lattice of voids, which is eventually squeezed out at densities near n_0 , as described in Ref. 12. If so, beginning at about $0.1n_0$, there could be a continuous change of the dimensionality of matter from 3-D nuclei (meatballs), to 2-D cylindrical nuclei (spaghetti),

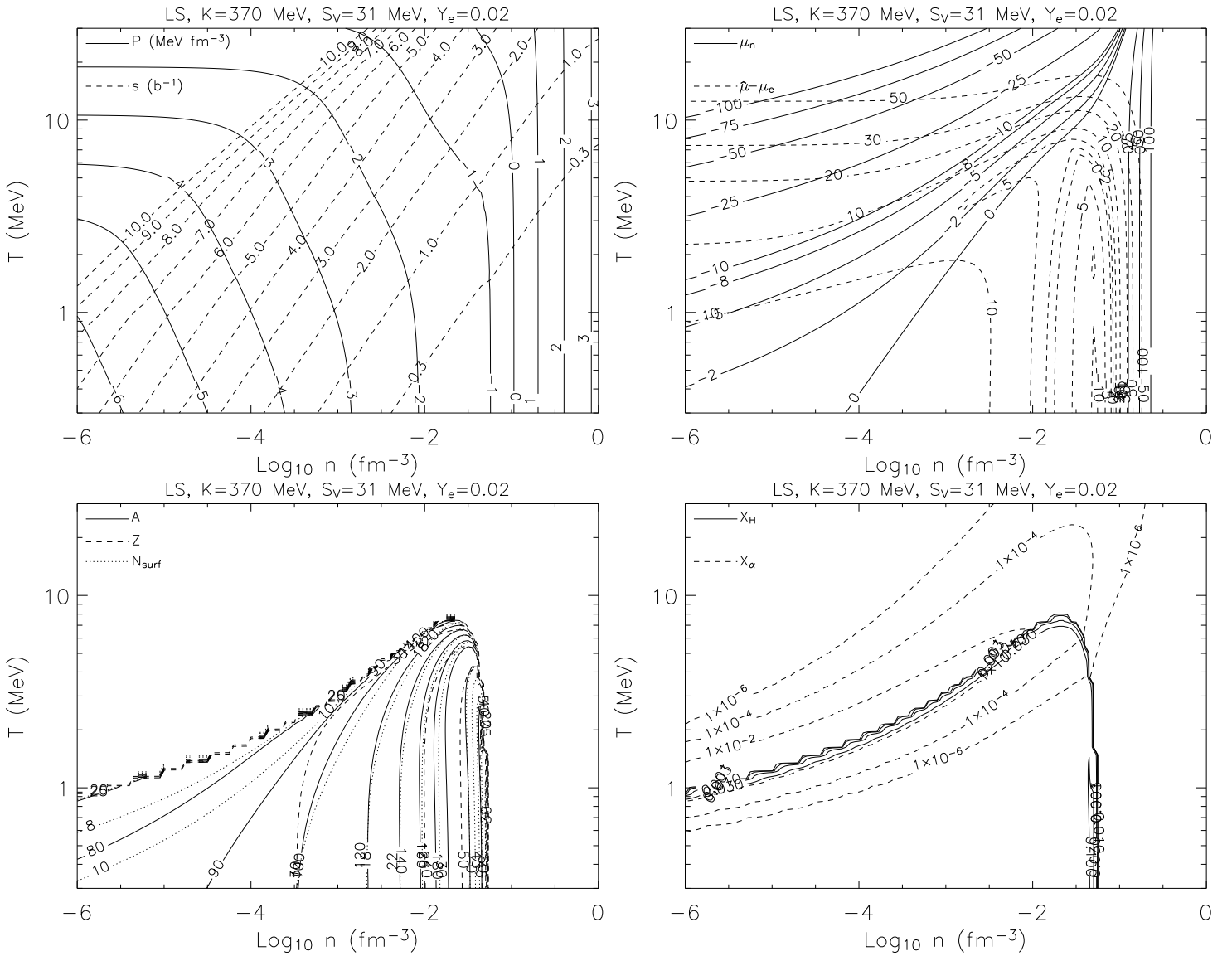


Figure 2.5: Same as Fig. 2.4, but for $Y_e = 0.02$.

to 1-D slabs of nuclei interlaid with planar voids (lasagna), to 2-D cylindrical voids (ziti), to 3-D voids (ravioli, or Swiss cheese in Fig. 3.1 before an eventual transition to uniform nucleonic matter (sauce). This series of transitions is thus known as the “nuclear pasta”.

It seems likely that for temperatures smaller than about 0.1 MeV the neutron fluid in the crust forms a 1S_0 superfluid. This is important because, first, it would alter the specific heat and the neutrino emissivities of the crust, thereby affecting how neutron stars cool. Second, it would form a reservoir of angular momentum that, being loosely coupled to the crust, could play a major role in pulsar glitch phenomena.

The core comprises nearly all the mass of the star. At least in its outer portion, it consists of a soup of nucleons, electrons and muons. The neutrons could form a 3P_2 superfluid and the protons a 1S_0 superconductor within the outer core. In the inner core exotic particles such as strangeness-bearing hyperons and/or Bose condensates (pions or kaons) may become abundant. It is even possible that a transition to a mixed phase of

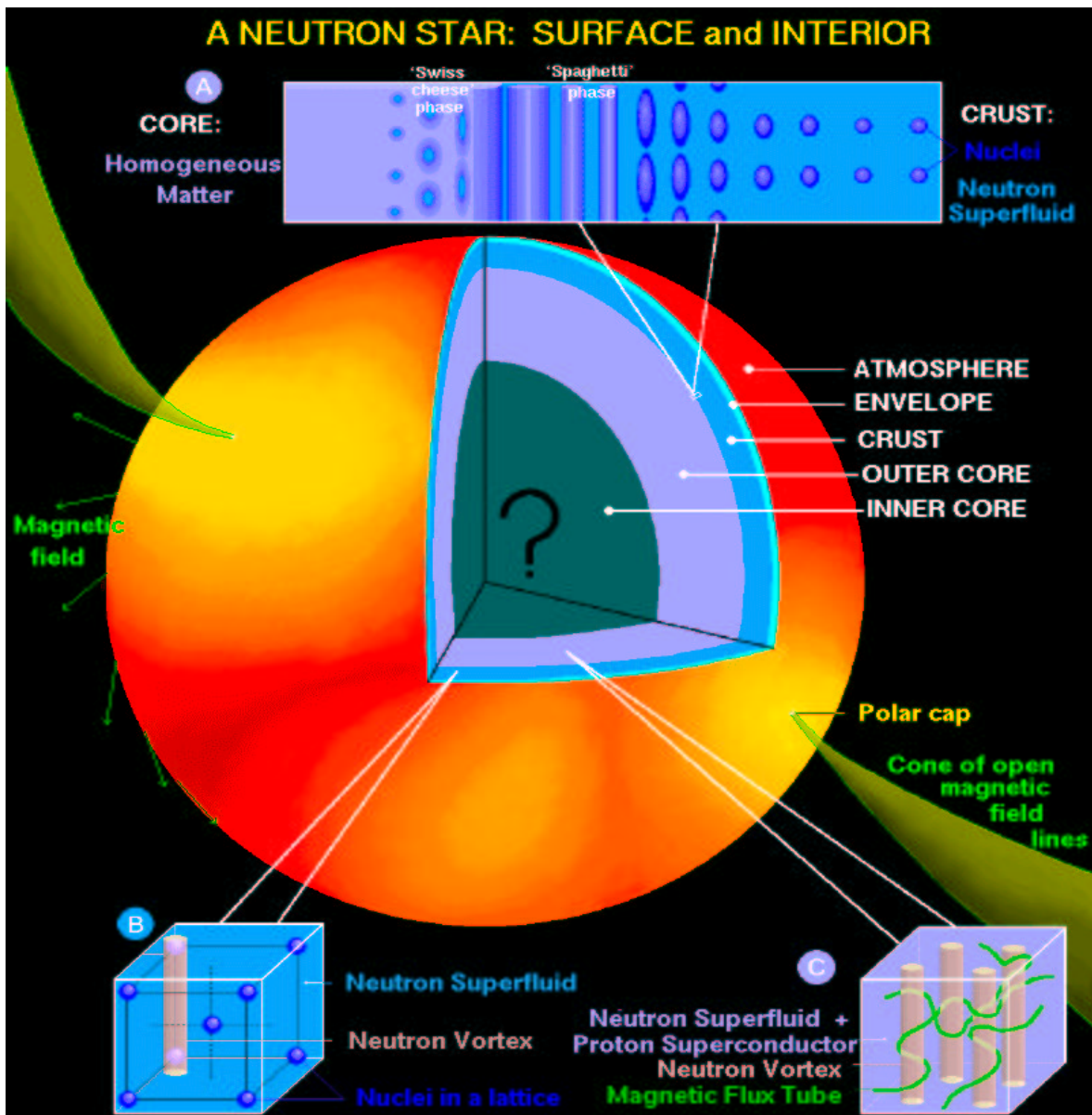


Figure 3.1: The internal composition of a neutron star. The top band illustrates the geometric transitions that might occur, from uniform matter at high densities, to spherical nuclei at low densities. Superfluid aspects of the crust and core are shown in insets.

hadronic and deconfined quark matter develops, even if strange quark matter is not the ultimate ground state of matter. Recent years have seen intense activity in delineating the phase structure of dense cold quark matter. Novel states of matter uncovered so far include color-superconducting phases with and without condensed mesons. Examples in the former case include a two-flavor superconducting (2SC) phase, a color-flavor-locked (CFL) phase, a crystalline phase, and a gapless superconducting phase. The densities at which these phases occur are still somewhat uncertain. In quark phases with finite gaps, initial estimates indicate gaps of several tens of MeV or more in contrast to gaps of a few MeV in baryonic phases.

3.1. Crustal Neutron Star Matter: $n < n_0$

It is instructive to examine some consequences of the equilibrium conditions derived above as they pertain to the composition of matter in the crust of a neutron star, i.e., where the density $n < n_0$. A cold neutron star is in beta equilibrium, since neutrinos can freely escape on the timescales of interest. In such matter, the optimum composition is obtained by finding the optimum value of Y_e by free energy minimization, which results in

$$\hat{\mu} = \mu_e = \hbar c (3\pi^2 n Y_e)^{1/3}, \quad (3.1)$$

where the electrons are assumed to be degenerate and relativistic. For the SKM* interaction, the beta-equilibrium properties of the matter are shown in Fig. 3.2. Note that at zero temperature, Y_e has a minimum in the vicinity of $0.02n_0$ with a value of about 0.02. Also, the abundance of heavy nuclei abruptly decreases above 10^{-4} fm^{-3} . Details of the nuclear composition are shown in Fig. 3.3; it is apparent that the nuclear mass number steadily increases with density until nuclei dissolve around 0.02 fm^{-3} . (This value of density marks the minimum value of Y_e .)

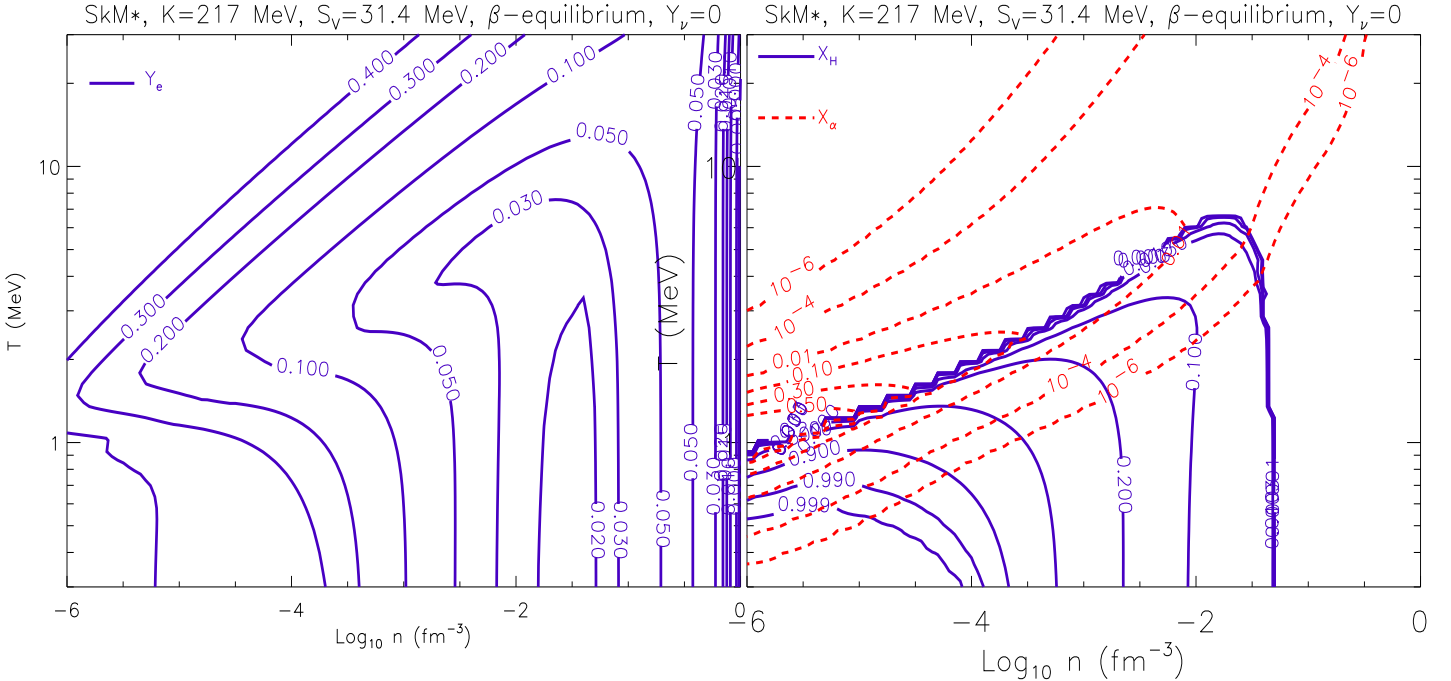


Figure 3.2: Beta equilibrium matter for the SKM* interaction. Left panel: Y_e contours. Right panel: nuclear X_H and α particle X_α abundances.

The pressure condition, and the relatively large value of the incompressibility parameter K , ensures, first of all, that the density inside nuclei will remain close to n_0 irrespective of the overall matter density n . The proton fraction inside nuclei, however, will vary more. In beta equilibrium, using the schematic interaction Eq. (2.24), and assuming that the abundance of outside nucleons is very small, the liquid droplet model predicts

$$4S_v(1 - 2x_I) + \frac{3}{5}x_I D \frac{4n_I}{3\pi^2 A} = \hbar c (3\pi^2 n x_I)^{1/3}, \quad (3.2)$$

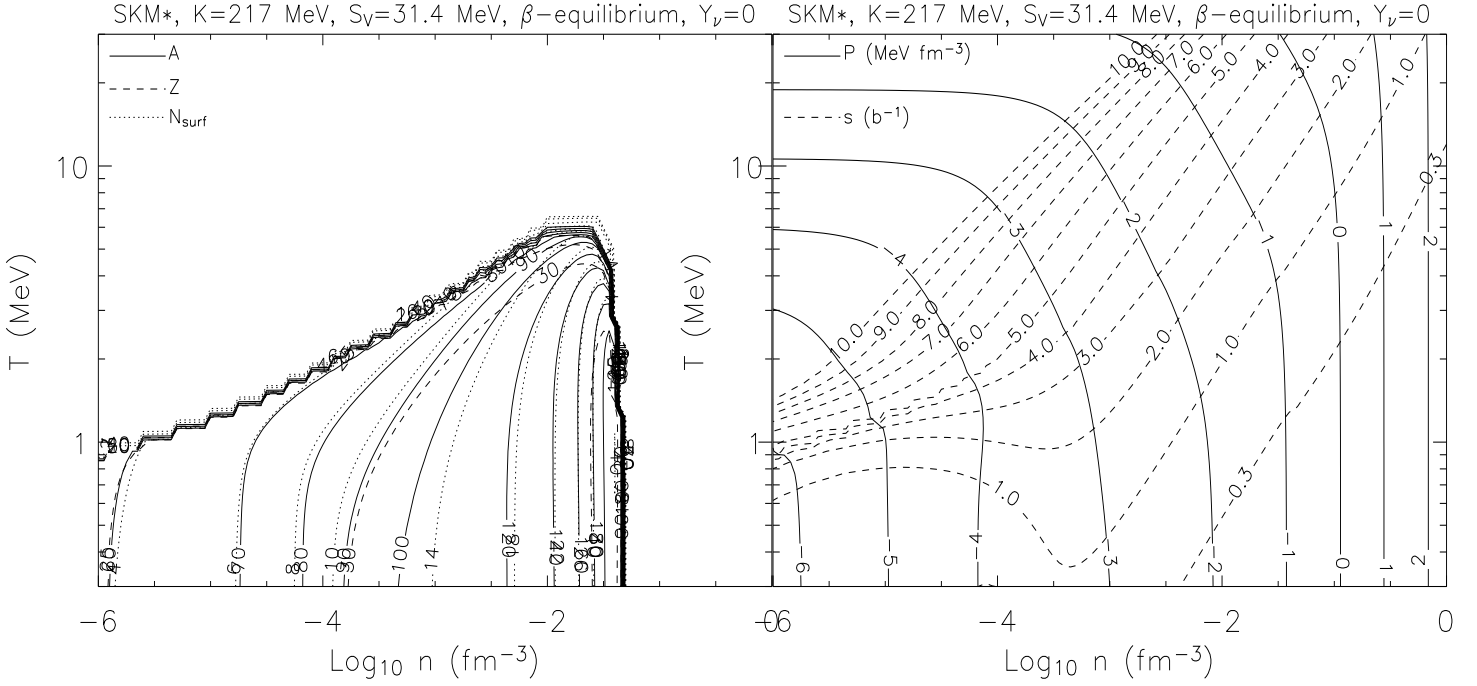


Figure 3.3: Beta equilibrium matter for the SKM* interaction. Left panel: A and Z contours. Right panel: pressure and entropy contours.

$$A = \frac{5\pi}{2n_I x_I^2 e^2 D} \left[\sigma_0 - \sigma_\delta (1 - 2x_I)^2 \right]. \quad (3.3)$$

According to Eq. (3.2), as the density n increases, x_I must decrease, as observed in Fig. 3.2 (recall that $Y_e \simeq x_I$). As a result, A increases. Around the density $n \approx 10^{-4}n_0$, the neutron chemical potential becomes positive. From Eq. (2.25), one has

$$x_d \simeq \frac{1}{2} \sqrt{1 + \frac{B}{2S_v}} \simeq 0.41. \quad (3.4)$$

The linear symmetry energy overestimates x_d compared to the models shown in Fig. 3.2. The “neutron drip point” is the density where $Y_e \simeq x_d$. Above this density, neutrons flood out of nuclei.

3.2. Ultra-High Density Matter

Despite the existence of many models of nuclear matter that successfully predict several aspects of nuclear structure, extrapolating these interactions to twice nuclear density and beyond, or to proton fractions below 0.4, is dangerous. From a practical standpoint, we have two constraints, namely causality and the existence of neutron stars of at least $1.44 M_{\odot}$. Nevertheless, a lot of freedom still exists. A survey of many often-used nuclear forces is described in Ref. 16. In Fig. 3.4, we compare the pressure-density relations of beta-equilibrium neutron star matter for some of these models.

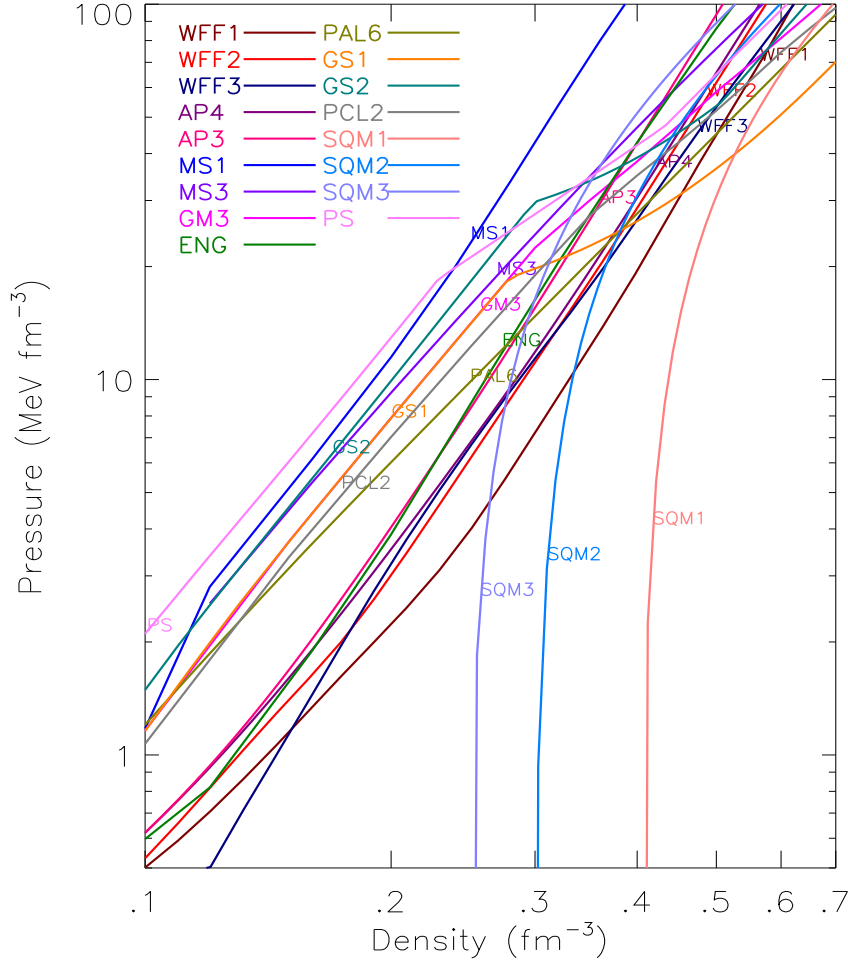


Figure 3.4: Pressure-density relation for EOS's described in Ref. 16.

The figure notes a number of important points. First, the effective polytropic index $n = \partial P / \partial \rho - 1$ of most normal nuclear EOS's is about 1. From the Newtonian equation of hydrostatic equilibrium, dimensional analysis shows that the stellar radius of an object with a constant polytropic index varies in a power law fashion with mass and the constant K in the polytrope law:

$$R \propto K^{n/(e-n)} M^{(1-n)/(3-n)}, \quad P = K \rho^{n+1}. \quad (3.5)$$

Second, at nuclear saturation density, $n_0 \simeq 0.16 \text{ fm}^{-3}$, and for normal EOS's, the uncertainty in the pressure is about a factor of 6. It is easily seen that the pressure of matter

in the vicinity of n_0 is completely determined by the symmetry parameter S_v and its density dependence. Using, for example, the schematic expansion Eq. (2.24), the pressure is given in Eq. (2.25). Obviously, when $n = n_0$, the pressure at zero temperature is $S_v n_0$ for neutron-rich matter. The schematic energy density in Eq. (2.24) utilized a linearly-varying symmetry energy per particle. In practice, this might be somewhat too steep. For one thing, the kinetic energy density of the fermionic baryons has a symmetry energy contribution that scales as $n^{2/3}$. In general, if the symmetry energy scales as n^p , then the pressure of pure neutron matter at n_0 is $p n_0 S_v$. According to the scaling in Eq. (3.5), one might anticipate that the radius of a star constructed with a weaker symmetry energy would be smaller than one constructed with a stronger symmetry dependence. This is actually true in practice, as we will observe in the next chapter. The fact that the pressure is uncertain is a direct statement about our lack of knowledge of the symmetry energy's density dependence, and leads to about a 50% uncertainty in the predicted neutron star radius.

Third, the strange-quark matter EOS's, which have a finite density at zero pressure, have a completely different low-density behavior than normal matter EOS's. This will lead to significant differences in the structure of pure strange quark matter stars.

Fourth, it should be noted that many normal EOS's display significant softening (flattening) of the pressure-density relation in the range $2 - 4n_0$. This behavior has consequences for limiting the value of the neutron star maximum mass.

4. Neutron Star Structure

Newtonian hydrostatic equilibrium, which is adequate for most stars, breaks down for neutron stars. Probably the most important defect is the inability to predict the existence of the maximum mass. Compactness limits were described over 200 years ago by Laplace, who demonstrated that the escape velocity $\sqrt{GM/R}$ could eventually exceed the speed of light. Surprisingly, this limit carries over into general relativity (GR), but in addition, GR predicts a number of further constraints on compactness. Besides the additional limit imposed on the mass, GR also predicts that the measurement of any neutron star mass leads to a limit on the maximum density inside *any* neutron star, and is thus a limit to the ultimate energy density of cold, static, matter in our universe.

4.1. General Relativistic Structure Equations

We confine attention to spherically symmetric configurations. The metric for the static case can generally be written

$$ds^2 = e^{\lambda(r)} dr^2 + r^2 (d\theta^2 + \sin^2 \theta d\phi^2) - e^{\nu(r)} dt^2. \quad (4.1)$$

The functions $\lambda(r)$ and $\nu(r)$ are referred to as metric functions. As derived in any text on GR, Einstein's equations for this metric are:

$$\begin{aligned} 8\pi\rho(r) &= \frac{1}{r^2} (1 - e^{-\lambda}) + e^{-\lambda} \frac{\lambda'(r)}{r}, \\ 8\pi p(r) &= -\frac{1}{r^2} (1 - e^{-\lambda}) + e^{-\lambda} \frac{\nu'(r)}{r}, \\ p'(r) &= -\frac{p(r) + \rho(r)}{2} \nu'(r). \end{aligned} \quad (4.2)$$

Derivatives with respect to the radius are denoted by $'$. We employ units in which $G = c = 1$, so that $1 M_{\odot}$ is equivalent to 1.475 km. The first of Eq. (4.2) can be exactly integrated. Defining the constant of integration so obtained as $m(r)$, the enclosed gravitational mass, one finds

$$e^{-\lambda} = 1 - 2m(r)/r, \quad m(r) = 4\pi \int_0^r \rho r'^2 dr'. \quad (4.3)$$

The second and third of Einstein's equations form the equation of hydrostatic equilibrium, also known as the Tolman-Oppenheimer-Volkov (TOV) equation in GR:

$$\frac{-p'(r)}{\rho(r) + p(r)} = \frac{\nu'(r)}{2} = \frac{m(r) + 4\pi r^3 p(r)}{r(r - 2m(r))}. \quad r \leq R \quad (4.4)$$

Near the origin, one has $\rho'(r) = p'(r) = m(r) = 0$. Outside the distribution of mass, which terminates at the radius R , there is vacuum with $p(r) = \rho(r) = 0$, and Einstein's equations give

$$m(r) = m(R) \equiv M, \quad e^{\nu} = e^{-\lambda} = 1 - \frac{2M}{r}, \quad r \geq R \quad (4.5)$$

the so-called Schwarzschild exterior solution. The black hole limit is seen to be $R = 2M$, which is 2.95 km for $1 M_{\odot}$, exactly the limit deduced by Laplace.

From thermodynamics, if there is uniform entropy per nucleon, the first law gives

$$0 = d\left(\frac{\rho}{n}\right) + pd\left(\frac{1}{n}\right)$$

where n is the number density. If e is the internal energy per nucleon, we have $\rho = n(m+e)$. From the above, $p = n^2 de/dn$, so that

$$d(\log n) = \frac{d\rho}{\rho + p} = -\frac{1}{2} \frac{d\rho}{dP} d\nu, \quad dn = \frac{d\rho}{h},$$

where $h = (\rho + p)/n$ is the enthalpy per nucleon or the chemical potential. The constant of integration for the number density can be established from conditions at the surface of the star, where the pressure vanishes (it is not necessary that the energy density or the number density also vanish there). If $n = n_o, \rho = \rho_o$ and $e = e_o$ when $P = 0$, one finds $\rho_o - mn_o = n_o e_o$ and

$$mn(r) = (\rho(r) + p(r)) e^{(\nu(r) - \nu(R))/2} - n_o e_o. \quad (4.6)$$

Another quantity of interest is the total number of nucleons in the star, N . This is not just M/m_b (m_b being the nucleon mass) since in GR the binding energy represents a decrease of the gravitational mass. The nucleon number is

$$N = \int_0^R 4\pi r^2 e^{\lambda/2} n(r) dr = \int_0^R 4\pi r^2 n(r) \left[1 - \frac{2m(r)}{r}\right]^{-1/2} dr, \quad (4.7)$$

and the total binding energy is

$$BE = Nm_b - M. \quad (4.8)$$

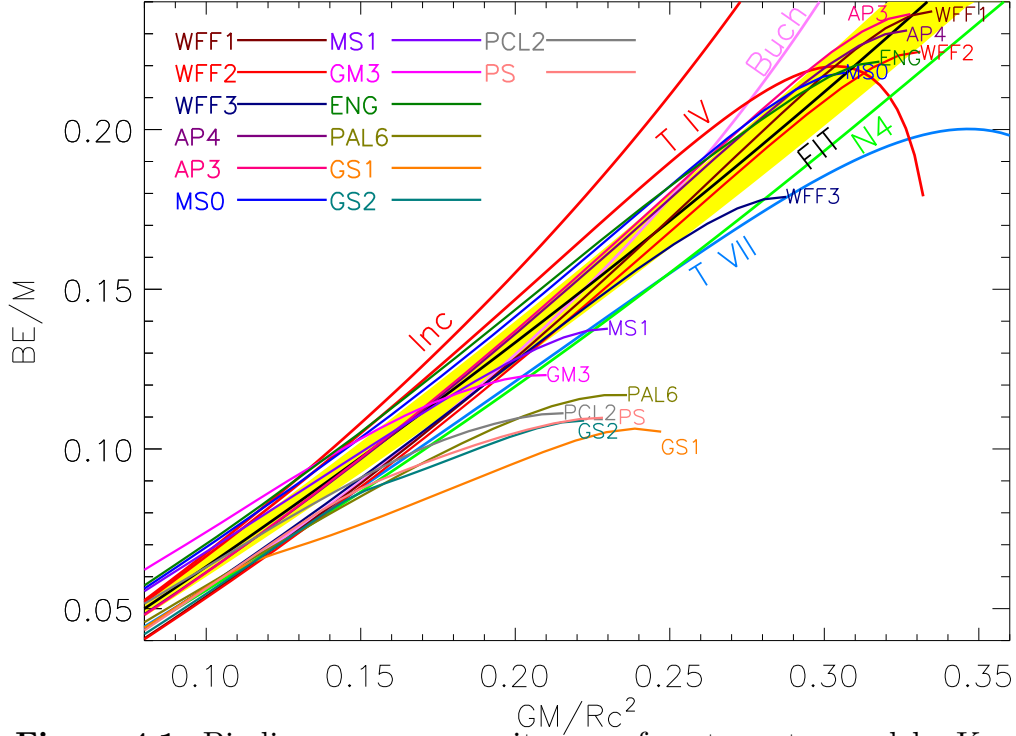


Figure 4.1: Binding energy per unit mass of neutron star models. Key to EOS's is in Ref. 16. The thicker curves with larger text symbols represent various analytic solutions. The yellow shaded band indicates approximation of Eq. (4.9).

Lattimer and Prakash¹⁶ gave an approximate relation between BE and M/R as

$$BE/M \simeq 0.6\beta / (1 - 0.5\beta), \quad (4.9)$$

which is shown in Fig. 4.1 along with representative EOS's and analytical solutions.

The moment of inertia of a star in the limit of a small rotation rate Ω is obtained from the expression

$$I = \frac{8\pi}{3} \int_0^R r^4 (\rho + P) e^{(\lambda-\nu)/2} \frac{\bar{\omega}}{\Omega} dr, \quad (4.10)$$

where the metric function $\bar{\omega}$ is a solution of

$$d \left[r^4 e^{-(\lambda+\nu)/2} \frac{d\bar{\omega}}{dr} \right] + 4r^3 \bar{\omega} de^{-(\lambda+\nu)/2} = 0 \quad (4.11)$$

with the surface boundary condition

$$\bar{\omega} = \Omega - \frac{R}{3} \left(\frac{d\bar{\omega}}{dr} \right)_R = \Omega \left(1 - \frac{2I}{R^3} \right). \quad (4.12)$$

It is convenient to define $j = \exp[-(\lambda + \nu)/2]$. Then,

$$I = -\frac{2}{3} \int_{r=0}^{r=R} \frac{\bar{\omega}}{\Omega} dj = \frac{R^4}{6\Omega} \left(\frac{d\bar{\omega}}{dr} \right)_R. \quad (4.13)$$

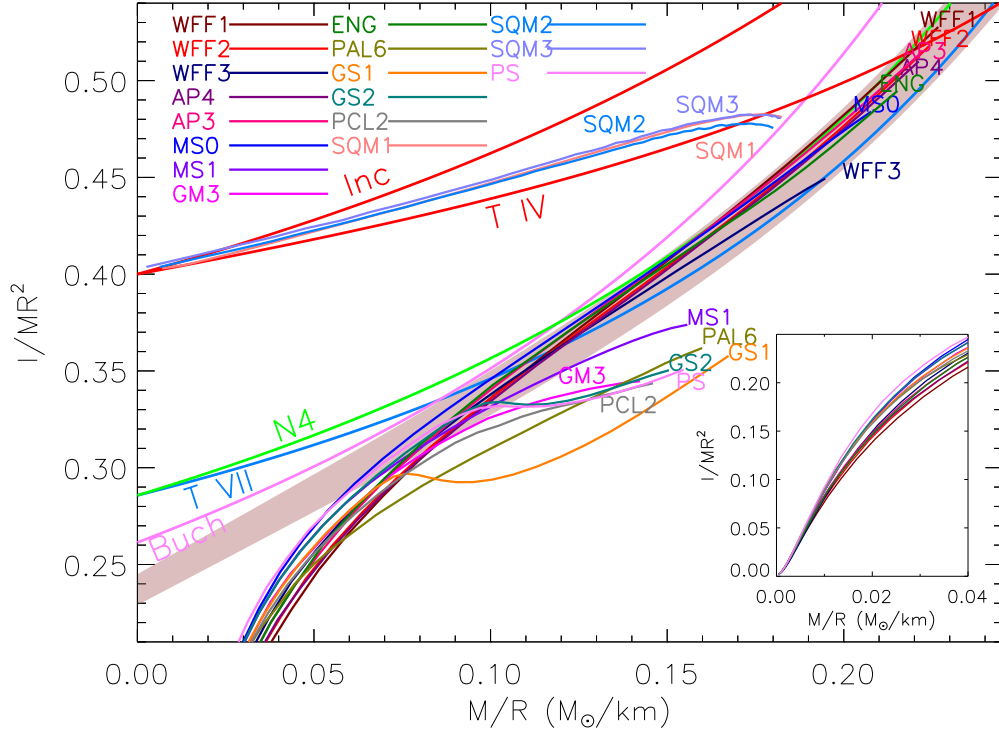


Figure 4.2: Moments of inertia of neutron star models. Key to EOS's is in Ref. 16. The thicker curves with larger text symbols represent various analytic solutions. The shaded gray band indicates the approximation Eq. (4.14). Inset shows the behavior for small M/R .

In practice, one integrates the dimensionless second order equation found from Eq. (4.11),

$$d \left[\xi^4 j \frac{d\omega}{d\xi} \right] + 4\xi^3 \omega dj = 0,$$

where $\xi = r/R$, from the origin where the initial values $\omega(0) = \bar{\omega}(0)/\Omega = 1$ and $d\omega(0)/d\xi = 0$, to $\xi = 1$. Then application of the surface boundary condition, Eq. (4.12), yields

$$\frac{I}{MR^2} = \frac{1}{\beta} \left(\frac{d\omega}{d\xi} \right)_1 \frac{1}{6\omega_1 + 2(d\omega/d\xi)_1},$$

where we use the values ω_1 and $(d\omega/d\xi)_1$ obtained at $\xi = 1$. Lattimer and Schutz¹⁷ found an approximation valid for normal EOS's that don't display severe softening just above n_0 :

$$I \simeq (0.237 \pm 0.008) MR^2 \left[1 + 4.2 \frac{M \text{ km}}{R M_\odot} + 90 \left(\frac{M \text{ km}}{R M_\odot} \right)^4 \right]. \quad (4.14)$$

This is shown in Fig. 4.2 together with representative EOS's and analytic solutions.

4.2. Mass-Radius Diagram for Neutron Stars

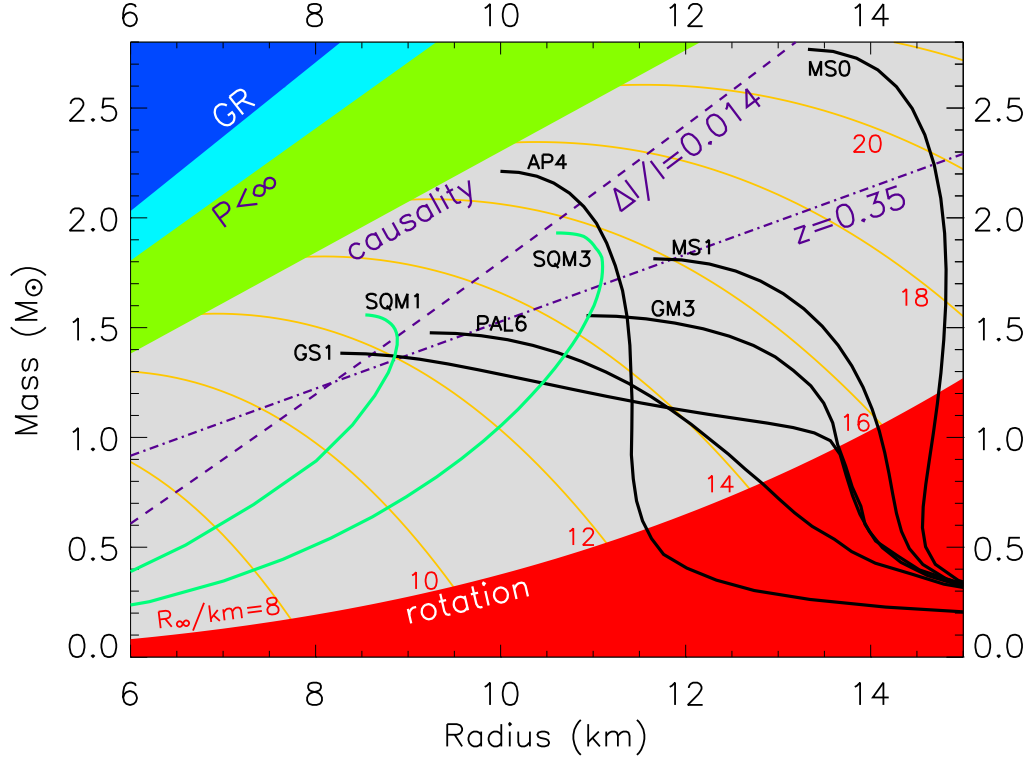


Figure 4.3: Mass-Radius diagram. The lines denoted GR, $P < \infty$, and causality represent limits to physically realistic structures (see text). Black curves are for normal nucleonic EOS's, while green curves (SQM1 and SQM3) are for pure strange quark matter stars. The notation for the EOS's is detailed in Ref. 16. The red region labeled rotation shows a limit derived from the most rapidly rotating pulsar. Orange curves are contours of radiation radii $R_\infty = R/\sqrt{1 - 2GM/R}$. The dashed line is a limit derived from Vela pulsar glitches, while $z = 0.35$ is the redshift of candidate spectral lines on a neutron star.

Given the relation $P(\rho)$ where ρ is the mass-energy density, the TOV equations can be integrated. Fig. 4.3 shows the mass as a function of radius for selected EOS's. Note the dramatic differences among normal EOS's, and also the difference between normal and strange quark matter EOS's. The presence of a maximum mass for each EOS is apparent. In addition, there is a minimum mass as well, with a value of approximately $0.09 M_\odot$, but this is not displayed since R_{min} is of order 200 km. It is interesting to note that many normal nucleonic EOS's have the property that in the mass range near $1 M_\odot$ the radius is relatively independent of the mass. This behavior is related to the approximate $n = 1$ polytrope behavior observed previously.

4.3. Analytic Solutions to Einstein's Equations

It turns out there are hundreds of analytic solutions to Einstein's equations. However, there are only 3 that satisfy the criteria that the pressure and energy density vanish on the boundary R , and that the pressure and energy density decrease monotonically with increasing radius. These are discussed below, together with two of the infinite number of known solutions that have vanishing pressure, but not energy density, at R .

4.3.1. Uniform density model

Among the simplest analytic solutions is the so-called Schwarzschild interior solution for a constant density fluid, $\rho(r) = \text{constant}$. In this case,

$$\begin{aligned}
 m(r) &= \frac{4\pi}{3}\rho r^3, & e^{-\lambda} &= 1 - 2\beta (r/R)^2, \\
 e^\nu &= \left[\frac{3}{2}\sqrt{1-2\beta} - \frac{1}{2}\sqrt{1-2\beta (r/R)^2} \right]^2, \\
 p(r) &= \frac{3\beta}{4\pi R^2} \frac{\sqrt{1-2\beta (r/R)^2} - \sqrt{1-2\beta}}{3\sqrt{1-2\beta} - \sqrt{1-2\beta (r/R)^2}}, \\
 \rho &= n(m+e) = \text{constant}, & n &= \text{constant}.
 \end{aligned} \tag{4.15}$$

Here, $\beta \equiv M/R$. Clearly, $\beta < 4/9$ or else the denominator has a zero and the central pressure will become infinite. It can be shown that this limit to β holds for *any* star. This solution is technically unphysical for the reasons that the energy density does not vanish on the surface, and that the speed of sound, $c_s = \sqrt{\partial p / \partial \rho}$ is infinite. The binding energy for the incompressible fluid is analytic (taking $e = 0$):

$$\frac{BE}{M} = \frac{3}{4\beta} \left(\frac{\sin^{-1} \sqrt{2\beta}}{\sqrt{2\beta}} - \sqrt{1-2\beta} \right) - 1 \simeq \frac{3\beta}{5} + \frac{9\beta^2}{14} + \dots \tag{4.16}$$

In the case that e/m is finite, the expansion becomes

$$\frac{BE}{M} \simeq \left(1 + \frac{e}{m} \right)^{-1} \left[-\frac{e}{m} + \frac{3\beta}{5} + \frac{9\beta^2}{14} + \dots \right]. \tag{4.17}$$

The moment of inertia can be approximated as

$$I_{Inc}/MR^2 \simeq (2/5) (1 - 0.87\beta - 0.3\beta^2)^{-1}. \tag{4.18}$$

4.3.2. Buchdahl's solution

In 1967, Buchdahl¹⁸ discovered an extension of the Newtonian $n = 1$ polytrope into GR that has an analytic solution. He assumed an equation of state

$$\rho = 12\sqrt{p_*p} - 5p \quad (4.19)$$

and found

$$\begin{aligned} e^\nu &= (1 - 2\beta)(1 - \beta - u)(1 - \beta + u)^{-1}; \\ e^\lambda &= (1 - 2\beta)(1 - \beta + u)(1 - \beta - u)^{-1}(1 - \beta + \beta \cos Ar')^{-2}; \\ 8\pi p &= A^2 u^2 (1 - 2\beta)(1 - \beta + u)^{-2}; \\ 8\pi \rho &= 2A^2 u (1 - 2\beta)(1 - \beta - 3u/2)(1 - \beta + u)^{-2}; \\ mn &= 12\sqrt{pp_*} \left(1 - \frac{1}{3}\sqrt{\frac{p}{p_*}}\right)^{3/2}; \quad c_s^2 = \left(6\sqrt{\frac{p_*}{p}} - 5\right)^{-1}. \end{aligned} \quad (4.20)$$

Here, p_* is a parameter, and r' is, with u , a radial-like variable

$$\begin{aligned} u &= \beta (Ar')^{-1} \sin Ar'; \\ r' &= r (1 - \beta + u)^{-1} (1 - 2\beta); \\ A^2 &= 288\pi p_* (1 - 2\beta)^{-1}. \end{aligned} \quad (4.21)$$

This solution is limited to values of $\beta < 1/6$ for $c_{s,c} < 1$. For this solution, the radius, central pressure, energy and number densities, and binding energy are

$$\begin{aligned} R &= (1 - \beta) \sqrt{\frac{\pi}{288p_*(1 - 2\beta)}}; \\ p_c &= 36p_*\beta^2; \quad \rho_c = 72p_*\beta(1 - 5\beta/2); \quad n_c m_n c^2 = 72\beta p_* (1 - 2\beta)^{3/2}; \\ \frac{BE}{M} &= (1 - 1.5\beta)(1 - 2\beta)^{-1/2}(1 - \beta)^{-1} - 1 \approx \frac{\beta}{2} + \frac{\beta^2}{2} + \frac{3\beta^3}{4} + \dots \end{aligned} \quad (4.22)$$

The moment of inertia can be approximated as

$$I_{Buch}/MR^2 \simeq (2/3 - 4/\pi^2)(1 - 1.81\beta + 0.47\beta^2)^{-1}. \quad (4.23)$$

4.4. Tolman VII solution

In 1939, Tolman² discovered that the simple density function $\rho = \rho_c[1 - (r/R)^2]$ has an analytic solution. It is known as the Tolman VII solution:

$$\begin{aligned}
e^{-\lambda} &= 1 - \beta x(5 - 3x), & e^\nu &= (1 - 5\beta/3) \cos^2 \phi, \\
P &= \frac{1}{4\pi R^2} \left[\sqrt{3\beta e^{-\lambda}} \tan \phi - \frac{\beta}{2} (5 - 3x) \right], & n &= \frac{(\rho + P) \cos \phi}{m \cos \phi_1}, \\
\phi &= (w_1 - w)/2 + \phi_1, & \phi_c &= \phi(x=0), \\
\phi_1 &= \phi(x=1) = \tan^{-1} \sqrt{\beta/[3(1-2\beta)]}, \\
w &= \log \left[x - 5/6 + \sqrt{e^{-\lambda}/(3\beta)} \right], & w_1 &= w(x=1).
\end{aligned} \tag{4.24}$$

In the above, $x = (r/R)^2$. The central values of P/ρ and the square of the sound speed $c_{s,c}^2$ are

$$\left. \frac{P}{\rho} \right|_c = \frac{2c_{s,c}^2}{15} \sqrt{\frac{3}{\beta}}, \quad c_{s,c}^2 = \tan \phi_c \left(\tan \phi_c + \sqrt{\frac{\beta}{3}} \right). \tag{4.25}$$

This solution is limited to $\phi_c < \pi/2$, or $\beta < 0.3862$, or else P_c becomes infinite. For causality $c_{s,c} < 1$ if $\beta < 0.2698$. There is no analytic result for the binding energy, but in expansion

$$\frac{BE}{M} \approx \frac{11\beta}{21} + \frac{7187\beta^2}{18018} + \frac{68371\beta^3}{306306} + \dots \tag{4.26}$$

A fit to the moment of inertia is

$$I_{TVII}/MR^2 \simeq (2/7) (1 - 1.1\beta - 0.6\beta^{-2})^{-1}. \tag{4.27}$$

4.4.1. Nariai IV solution

In 1950, Nariai¹⁹ discovered yet another analytic solution. It is known as the Nariai IV solution, and is expressed in terms of a parametric variable r' :

$$\begin{aligned}
e^{-\lambda} &= \left(1 - \sqrt{3\beta} \left(\frac{r'}{R'}\right)^2 \tan f(r')\right)^2, & e^\nu &= (1 - 2\beta) \frac{e^2}{c^2} \left(\frac{\cos g(r')}{\cos f(r')}\right)^2, \\
f(r') &= \cos^{-1} e + \sqrt{\frac{3\beta}{4}} \left[1 - \left(\frac{r'}{R'}\right)^2\right], & g(r') &= \cos^{-1} c + \sqrt{\frac{3\beta}{2}} \left[1 - \left(\frac{r'}{R'}\right)^2\right], \\
r &= \frac{e}{c} \frac{r'}{\cos f(r')} \sqrt{1 - 2\beta}, \\
p(r') &= \frac{\cos f(r')}{4\pi R'^2} \frac{c^2}{e^2} \sqrt{3\beta} \left[\sqrt{2} \cos f(r') \tan g(r') \right. \\
&\quad \left. \left[1 - \sqrt{3\beta} \left(\frac{r'}{R'}\right)^2 \tan f(r')\right] - \sin f(r') \left[2 - \frac{3}{2} \sqrt{3\beta} \left(\frac{r'}{R'}\right)^2 \tan f(r')\right] \right], \\
\rho(r') &= \frac{\sqrt{3\beta}}{4\pi R'^2 \sqrt{1 - 2\beta}} \frac{c^2}{e^2} \\
&\quad \left[3 \sin f(r') \cos f(r') - \sqrt{\frac{3\beta}{4}} \left(\frac{r'}{R'}\right)^2 (3 - \cos^2 f(r')) \right], \\
m(r') &= \frac{r'^3}{R'^2} \frac{e \tan f(r')}{c \cos f(r')} \sqrt{3\beta(1 - 2\beta)} \left[1 - \sqrt{\frac{3\beta}{4}} \left(\frac{r'}{R'}\right)^2 \tan f(r')\right].
\end{aligned} \tag{4.28}$$

The quantities e and c are

$$\begin{aligned}
e^2 &= \cos^2 f(R') = \frac{2 + \beta + 2\sqrt{1 - 2\beta}}{4 + \beta/3} \\
c^2 &= \cos^2 g(R') = \frac{2e^2}{2e^2 + (1 - e^2)(7e^2 - 3)(5e^2 - 3)^{-1}}.
\end{aligned}$$

The pressure-density ratio and sound speed at the center are

$$\begin{aligned}
\frac{P_c}{\rho_c} &= \frac{1}{3} \left(\sqrt{2} \cot f(0) \tan g(0) - 2 \right), \\
c_{s,c}^2 &= \frac{1}{3} (2 \tan^2 g(0) - \tan^2 f(0)).
\end{aligned}$$

The central pressure and sound speed become infinite when $\cos g(0) = 0$ or when $\beta = 0.4126$, and the causality limit is $\beta = 0.223$. This solution is quite similar to Tolman VII. The leading order term in the binding energy is identical to Tolman VII, and the moment of inertia expansion is

$$I/MR^2 \simeq (2/7) (1 - 1.32\beta - 0.21\beta^2)^{-1}. \tag{4.29}$$

4.4.2. Tolman IV variant

Lake²⁰ discovered a variant of a solution Tolman discovered in 1939² and since known as the Tolman IV solution:

$$\begin{aligned}
e^\nu &= \frac{(2 - 5\beta + \beta x)^2}{4(1 - 2\beta)}, & e^{-\lambda} &= 1 - 2\beta x \left(\frac{2 - 2\beta}{2 - 5\beta + 3\beta x} \right)^{2/3}, \\
m &= \beta R x^{\frac{3}{2}} \left(\frac{2 - 2\beta}{2 - 5\beta + 3\beta x} \right)^{2/3}, \\
\rho &= \frac{1}{4\pi R^2} \beta \left(\frac{6 - 15\beta + 5\beta x}{2 - 5\beta + 3\beta x} \right) \left(\frac{2 - 2\beta}{2 - 5\beta + 3\beta x} \right)^{2/3}, \\
P &= \frac{1}{4\pi R^2} \frac{\beta}{2 - 5\beta + \beta x} \left[2 - (2 - 5\beta + 5\beta x) \left(\frac{2 - 2\beta}{2 - 5\beta + 3\beta x} \right)^{2/3} \right], \\
c_s^2 &= \frac{(2 - 5\beta + 3\beta x)}{5(2 - 5\beta + \beta x)^3} \left[\frac{(2 - 5\beta + 3\beta x)^{5/3}}{(2 - 2\beta)^{2/3}} + (2 - 5\beta)^2 - 5\beta^2 x^2 \right].
\end{aligned} \tag{4.30}$$

The central values of P/ρ and c_s^2 are

$$\frac{P_c}{\rho_c} = \frac{1}{3} \left[\frac{2}{(2 - 5\beta)^{1/3} (2 - 2\beta)^{2/3}} - 1 \right], \quad c_{s,c}^2 = \frac{1}{5} \left[\frac{1}{(2 - 5\beta)^{1/3} (2 - 2\beta)^{2/3}} + 1 \right]. \tag{4.31}$$

This solution has non-vanishing energy density at the surface where the pressure vanishes. The ratio of the surface to central energy densities is

$$\frac{\rho_{surf}}{\rho_c} = \frac{2}{3} (3 - 5\beta) \frac{(2 - 5\beta)^{2/3}}{(2 - 2\beta)^{5/3}}, \tag{4.32}$$

which is unity for $\beta \rightarrow 0$, and tends to zero for $\beta = 2/5$. The surface sound speed is

$$c_{s,surf}^2 = \frac{2 - 2\beta}{5(2 - 4\beta)^3} \left[2 - 2\beta + (2 - 5\beta)^2 - 5\beta^2 \right]. \tag{4.33}$$

A good approximation to the moment of inertia for this solution is

$$I/MR^2 = (2/5) (1 - 0.58\beta - 1.1\beta^3)^{-1}, \tag{4.34}$$

The central pressure, energy density and sound speed become infinite for $\beta \geq 2/5$, and $c_s(0) = c$ when $\beta \geq 0.3978$. On the other hand, $c_s(R) = c$ when $\beta = 0.3624$. In the limit of small β , the central and the surface sound speed are both $c_s^2 = 3/10$, which makes this an interesting solution to compare with strange quark matter stars. The sound speed at large densities in strange quark matter tends to $c_s^2 = 1/3$ because of asymptotic freedom.

4.5. Neutron Star Maximum Mass and Compactness Limit

The TOV equation can be scaled by introducing dimensionless variables:

$$p = q\rho_o, \quad \rho = d\rho_o, \quad m = z/\sqrt{\rho_o}, \quad r = x/\sqrt{\rho_o},$$

$$\frac{dq}{dx} = -\frac{(q+d)(z+4\pi dx^3)}{x(x-2z)}, \quad \frac{dz}{dx} = 4\pi dx^2 dx. \quad (4.35)$$

Rhoades and Ruffini²¹ showed that thecausally limiting equation of state

$$p = p_o + \rho - \rho_o \quad \rho > \rho_o \quad (4.36)$$

results in a neutron star maximum mass that is practically independent of the equation of state for $\rho < \rho_o$, and is

$$M_{max} = 4.2\sqrt{\rho_s/\rho_o} M_\odot. \quad (4.37)$$

Here $\rho_s = 2.7 \cdot 10^{14} \text{ g cm}^{-3}$ is the nuclear saturation density. One also finds for this equation of state that

$$R_{max} = 18.5\sqrt{\rho_s/\rho_o} \text{ km}, \quad \beta_{max} \simeq 0.33. \quad (4.38)$$

Since the most compact configuration is achieved at the maximum mass, this represents the limiting value of β for causality, as Lattimer et al.²² pointed out. This result wasreinforced by Glendenning²³, who performed aparametrized variational calculation to find the most compace possible stars as a function of mass..

Some justification for the Rhoades-Ruffini result appears from the analytic solutions of Einstein's equations. For the Buchdahl solution at the causal limit, $\beta = 1/6$ and $p/\rho = \beta/(2 - 5\beta)$, which lead to

$$M = (1 - \beta) \sqrt{\frac{\pi\beta^3(1 - 5\beta/2)}{4(1 - 2\beta)\rho_c}} < 2.14\sqrt{\rho_s/\rho_c} M_\odot.$$

For the Tolman VII solution at the causal limit, $\beta \simeq 0.27$ and $p/\rho = 2/(\sqrt{75}\beta) \simeq 0.44$, which lead to

$$M = \sqrt{\frac{15\beta^3}{8\pi\rho_c}} < 4.9\sqrt{\rho_s/\rho_c} M_\odot.$$

Finally, for the Nariai IV solution at the causal limit, $\beta \simeq 0.228$ and $p/\rho \simeq 0.246$, which lead to

$$M = \frac{\beta}{\cos f(R')} \sqrt{\frac{3^{3/2}\beta^{1/2} \sin f(0) \cos f(0)}{4\pi\rho_c}} < 3.4\sqrt{\rho_s/\rho_c} M_\odot.$$

4.6. Maximal Rotation Rates for Neutron Stars

The absolute maximum rotation rate is set by the “mass-shedding” limit, when the rotational velocity at the equatorial radius (R) equals the Keplerian orbital velocity $\Omega = \sqrt{GM/R^3}$, or

$$P_{min}^{rigid} = 0.55 \left(\frac{10 \text{ km}}{R} \right)^{3/2} \left(\frac{M}{M_{\odot}} \right)^{1/2} \text{ ms} \quad (4.39)$$

for a rigid sphere. However, the actual limit on the period is larger because rotation induces an increase in the equatorial radius. In the so-called Roche model, as described in Shapiro and Teukolsky²⁴ one treats the rotating star as being highly centrally compressed. For an $n = 3$ polytrope, $\rho_c/\bar{\rho} \simeq 54$, so this would be a good approximation. In more realistic models, such as $\rho = \rho_c[1 - (r/R)^2]$, for which $\rho_c/\bar{\rho} = 5/2$, and an $n = 1$ polytrope, for which $\rho_c/\bar{\rho} = \pi^2/3$, this approximation is not as good. Using it anyway, the gravitational potential near the surface is $\Phi_G = -GM/r$ and the centrifugal potential is $\Phi_c = -(1/2)\Omega^2 r^2 \sin^2 \theta$, and the equation of hydrostatic equilibrium is

$$(1/\rho) \nabla P = \nabla h = -\nabla \Phi_G - \nabla \Phi_c, \quad (4.40)$$

where $h = \int dP/\rho$ is the enthalpy per unit mass. Integrating this from the surface to an interior point along the equator, one finds

$$h(r) - GM/r - (1/2)\Omega^2 r^2 = K = -GM/r_e - (1/2)\Omega^2 r_e^2,$$

where r_e is the equatorial radius and $h(r_e) = 0$. We assume $K = -GM/R$, the value obtained for a non-rotating configuration. The potential $\Phi \equiv \Phi_G + \Phi_c$ is maximized at the point where $\partial\Phi/\partial r|_{r_c} = 0$, or where $r_c^3 = gM/\Omega^3$ and $\Phi = -(3/2)GM/r_c$. Thus, r_e has the largest possible value when $r_e = r_c = 3R/2$, or

$$\Omega^2 = \frac{GM}{r_c^3} = \left(\frac{2}{3} \right)^3 \frac{GM}{R^3}. \quad (4.41)$$

The revised minimum period then becomes

$$P_{min}^{Roche} = 1.0 \left(\frac{10 \text{ km}}{R} \right)^{3/2} \left(\frac{M}{M_{\odot}} \right)^{1/2} \text{ ms}. \quad (4.42)$$

Calculations including general relativity show that the minimum spin period for an equation of state, including the increase in maximum mass for a rotating fluid, can be accurately expressed in terms of its *non-rotating* maximum mass and the radius at that maximum mass as:

$$P_{min}^{EOS} \simeq 0.82 \pm 0.03 \left(\frac{10 \text{ km}}{R_{max}} \right)^{3/2} \left(\frac{M_{max}}{M_{\odot}} \right)^{1/2} \text{ ms}. \quad (4.43)$$

An even more useful form describes the maximum rotation rate that a non-rotating object of mass M and radius R can be spun:

$$P_{min}^{arbitrary} \simeq 0.96 \pm 0.03 \left(\frac{10 \text{ km}}{R} \right)^{3/2} \left(\frac{M}{M_{\odot}} \right)^{1/2} \text{ ms}, \quad (4.44)$$

a result found to be valid for normal EOS's²⁵. It is moderately violated for strange quark-matter stars. It is this limit that is plotted in Fig. 4.3, using the highest observed spin period of a pulsar, 641 Hz from PSR B1937+21.

It is interesting to compare the rotational kinetic energy $T = I\Omega^2/2$ with the gravitational potential energy W at the mass-shedding limit. I is the moment of inertia about the rotation axis:

$$I = \frac{8\pi}{3} \int_0^R r^4 \rho dr$$

for Newtonian stars. (In GR, one must take into account frame-dragging as well as volume and redshift corrections.) Using $\Omega^2 = (2/3)^3 GM/R^3$, we can write $T = \alpha(2/3)^3 GM^2/R$ and $|W| = \beta GM^2/R$. We have $\alpha = 1/5, \beta = 3/5$ for an incompressible fluid; $\alpha = 1/3 - 2/\pi^2, \beta = 3/4$ for an $n = 1$ polytrope; $\alpha = 0.0377, \beta = 3/2$ for an $n = 3$ polytrope; $\alpha = 1/7, \beta = 5/7$ for Tolman VII for which $\rho = \rho_c[(1 - (r/R)^2)]$. We therefore find that $T/|W|$ is 0.0988, 0.0516, 0.00745 and 0.0593, respectively, for these four cases, at the mass-shedding limit. For comparison, an incompressible ellipsoid becomes secularly (dynamically) unstable at $T/|W| = 0.1375(0.2738)$, much larger values.

4.7. Maximum Density Inside Neutron Stars

If the uniform density model was a good model for a neutron star, the causality limit would imply a central density

$$\rho_{c,Inc} = \frac{3}{4\pi M^2} \left(\frac{c^2}{3G} \right)^3 \simeq 5.5 \times 10^{15} \left(\frac{M_\odot}{M} \right)^2 \text{ g cm}^{-3}. \quad (4.45)$$

A precisely measured neutron star mass would thus imply a value for the central density of the star. Furthermore, the larger the measured mass, the smaller the central density of that star. No other star, no matter what its mass, could have a central density larger than this value. A lower mass star cannot have a higher central density than that star, and if another star was more massive, it would have to have a *smaller* central density according to Eq. (4.45).

However, the uniform density EOS is not realistic: it violates causality and the density at the surface $\rho_{surface} \neq 0$. But, interestingly enough, a similar relation deduced from the Tolman VII analytic solution apparently bounds the relation between central density and maximum mass. By calculating the structures of a large number of neutron stars, Lattimer and Prakash²⁶ found no EOS has a greater ρ_c for given M_{max} than that predicted by the Tolman VII solution:

$$\rho_{c,VII} = \frac{5}{2} \rho_{c,Inc} \simeq 13.8 \times 10^{15} \left(\frac{M_\odot}{M} \right)^2 \text{ g cm}^{-3}. \quad (4.46)$$

This result is illustrated in Fig. 4.4, and can be used in the manner described above: the largest precisely measured neutron star mass determines an upper bound to the density of matter in a cold, static environment in our universe. Each larger mass star that is measured will lower this bound. The figure illustrates that a measured mass of about $2.2 M_\odot$ sets an upper bound of about $8n_0$, which is perhaps dangerously close to predicted

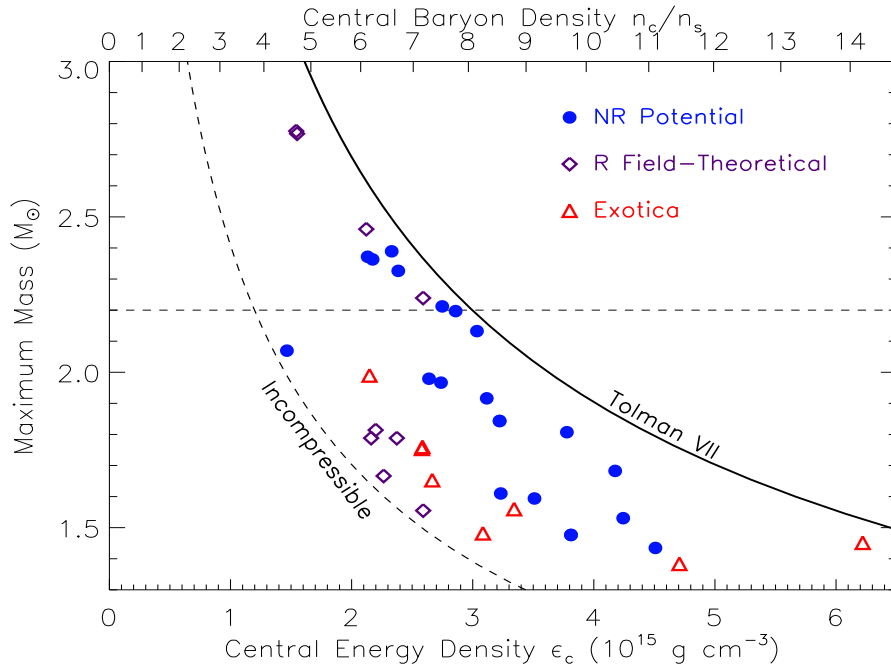


Figure 4.4: The central energy density and mass of maximum mass configurations. Symbols reflect the nature of the EOS’s selected from Ref. 16. NR are non-relativistic potential models, R are field- theoretical models, and Exotica refers to NR or R models in which strong softening occurs, due to the occurrence of hyperons, a Bose condensate, or quark matter. The Exotica points include self-bound strange quark matter stars. For comparison, the central density – maximum mass relations for the Tolman VII and uniform density (incompressible) models are shown. The dashed line for $2.2 M_{\odot}$ serves to guide the eye.

values for the density at which nucleonic matter gives way to deconfined quark matter. In other words, astrophysical measurements of neutron star masses may be able to rule out the existence of deconfined quark matter, at least in cold matter.

4.8. Neutron Star Radii

As previously noted, many EOS’s feature the property that in the vicinity of $1 M_{\odot}$ their radii are relatively independent of the mass. Polytropic relations Eq. (3.5) implied the value of the radius is connected to the constant K in the EOS, or to the value of the pressure at a characteristic density. Lattimer and Prakash¹⁶ found that, indeed, there is a strong correlation between the radius of stars with masses $1 - 1.5 M_{\odot}$ and the pressure in the vicinity of $1 - 2n_0$. This correlation is shown in Fig. 4.5.

The correlation has the form:

$$R(M, n) \simeq C(M, n) [P(n)]^{0.25}, \quad (4.47)$$

where $P(n)$ is the total pressure inclusive of leptonic contributions evaluated at the density n , and M is the stellar gravitational mass. The constant $C(M, n)$, in units of $\text{km fm}^{3/4}$

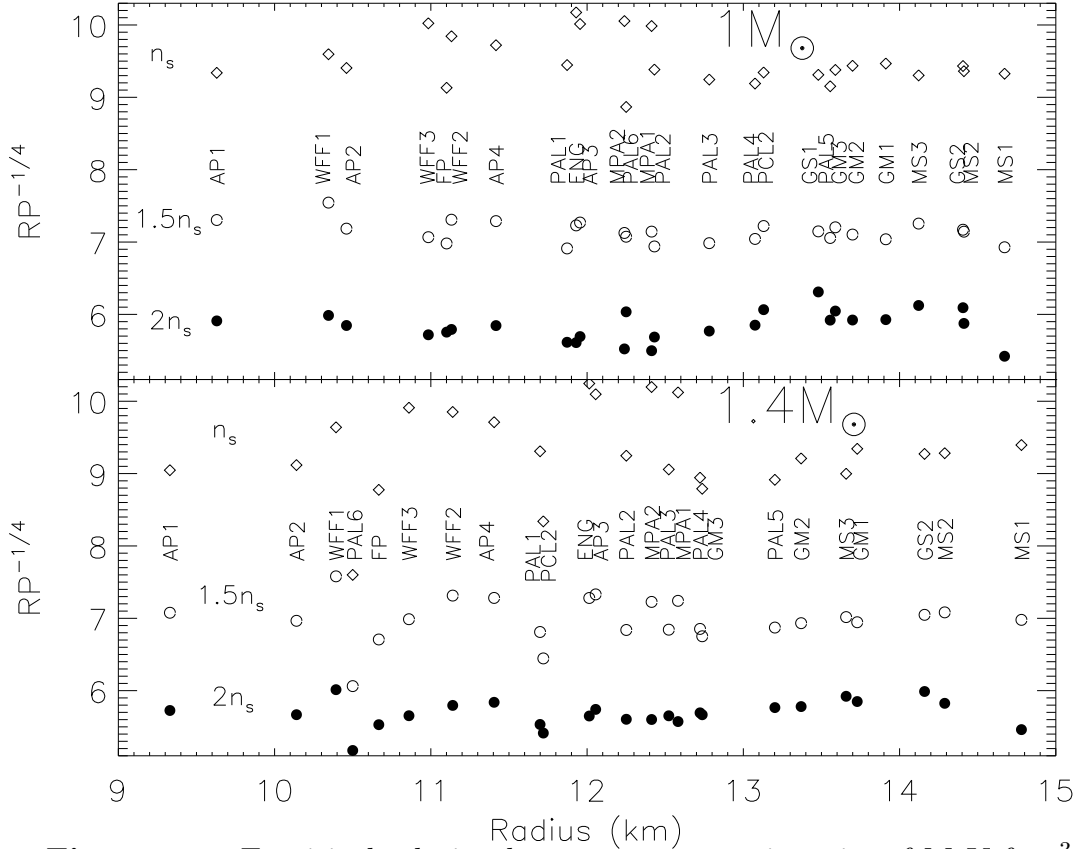


Figure 4.5: Empirical relation between pressure, in units of MeV fm^{-3} , and R , in km, for EOS's listed in Ref. 16. The upper panel shows results for $1 M_{\odot}$ (gravitational mass) stars; the lower panel is for $1.4 M_{\odot}$ stars. The different symbols show values of $RP^{-1/4}$ evaluated at three fiducial densities, n_0 , $1.5n_0$ and $2n_0$.

$\text{MeV}^{-1/4}$, for the densities $n = n_s$, $1.5n_s$ and $2n_s$, respectively, is 9.53 ± 0.07 , 7.16 ± 0.03 and 5.82 ± 0.04 for the $1 M_{\odot}$ case, and 9.11 ± 0.21 , 6.84 ± 0.15 and 5.57 ± 0.11 for the $1.4 M_{\odot}$ case. The correlation is seen to be somewhat tighter for the baryon density $n = 1.5n_s$ and $2n_s$ cases. Note, however, that this exponent is not $1/2$ as the $n = 1$ Newtonian polytrope predicts. This is a general relativistic effect, as we now demonstrate by using an analytic solution to Einstein's equations.

The only analytic solution that explicitly relates the radius, mass and pressure is that due to Buchdahl. In terms of the parameters p_* and $\beta \equiv GM/Rc^2$, the baryon density and stellar radius are given in Eqs. (4.20) and Eq. (4.22). The exponent in Eq. (4.47) can thus be found:

$$\left. \frac{d \ln R}{d \ln P} \right|_{n,M} = \frac{1}{2} \left(1 - \frac{5}{6} \sqrt{\frac{P}{p_*}} \right) \left(1 + \frac{1}{6} \sqrt{\frac{P}{p_*}} \right)^{-1} \frac{(1 - \beta)(1 - 2\beta)}{(1 - 3\beta + 3\beta^2)}. \quad (4.48)$$

In the limit $\beta \rightarrow 0$, one has $P \rightarrow 0$ and $d \ln R/d \ln P|_{n,M} \rightarrow 1/2$, the value characteristic of an $n = 1$ Newtonian polytrope. Finite values of β and P reduce the exponent. If M and R are about $1.4 M_{\odot}$ and 15 km, respectively, for example, $\beta \simeq 0.14$ and Eq. (4.22) gives

$p_* = \pi/(288R^2) \approx 4.85 \cdot 10^{-5} \text{ km}^{-2}$ (in geometrized units). At a fiducial density $n = 1.5n_s$, this is equivalent in geometrized units to $n = 2.02 \times 10^{-4} \text{ km}^{-2}$, or $n/p_* \simeq 4.2$. Eq. (4.20) then implies $P/p_* \simeq 0.2$ and Eq. (4.48) yields $d \ln R/d \ln P \simeq 0.28$.

This correlation is significant because the pressure of degenerate neutron-star matter near the nuclear saturation density n_s is, in large part, determined by the symmetry properties of the EOS. For the present discussion, we introduce an additional term, the skewness, and generalize the symmetry energy, in the schematic expansion Eq. (2.24), so that the energy per particle is

$$E(n, x) = -16 + \frac{K}{18} \left(1 - \frac{n}{n_0}\right)^2 + \frac{K'}{27} \left(1 - \frac{n}{n_0}\right)^3 + E_{sym}(n)(1 - 2x)^2 \dots \quad (4.49)$$

Here, K and K' are the incompressibility and skewness parameters, respectively, and E_{sym} is the symmetry energy function, approximately the energy difference at a given density between symmetric and pure neutron matter. The symmetry energy parameter $S_v \equiv E_{sym}(n_0)$. Leptonic contributions $E_e = (3/4)\hbar c x (3\pi^2 n x^4)^{1/3}$ must be added. Matter in neutron stars is in beta equilibrium, i.e., $\mu_e = \mu_n - \mu_p = -\partial E/\partial x$, so the equilibrium proton fraction at n_0 is $x_0 \simeq (3\pi^2 n_0)^{-1} (4S_v/\hbar c)^3 \simeq 0.04$. The pressure at n_0 is

$$P(n_0, x_0) = n_0(1 - 2x_0) [n_0 S'_v(1 - 2x_0) + S_v x_0] \simeq n_0^2 S'_v, \quad (4.50)$$

due the small value of x_0 ; $S'_v \equiv (\partial E_{sym}/\partial n)_{n_s}$. The pressure depends primarily upon S'_v . The equilibrium pressure at moderately larger densities similarly is insensitive to K and K' . Experimental constraints to the compression modulus K , most importantly from analyses of giant monopole resonances give $K \cong 220 \text{ MeV}$. The skewness parameter K' has been estimated to lie in the range 1780–2380 MeV. Evaluating the pressure for $n = 1.5n_0$,

$$P(1.5n_0) = 2.25n_0 \left[K/18 - K'/216 + n_0(1 - 2x)^2 (\partial E_{sym}/\partial n)_{1.5n_0} \right], \quad (4.51)$$

and it is noted that the contributions from K and K' largely cancel.

5. Observations of Neutron Stars

5.1. Masses

The most accurately measured neutron star masses are from timing observations of the radio binary pulsars. As shown in Fig. 5.1, these include pulsars orbiting another neutron star, a white dwarf or a main-sequence star. Ordinarily, observations of pulsars in binaries yield orbital sizes and periods from Doppler phenomenon, from which the total mass of the binary can be deduced. But the compact nature of several binary pulsars permits detection of relativistic effects, such as Shapiro delay or orbit shrinkage due to gravitational radiation reaction, which constrains the inclination angle and permits measurement of each mass in the binary. A sufficiently well-observed system can have masses determined to impressive accuracy. The textbook case is the binary pulsar PSR 1913+16, in which the masses are 1.3867 ± 0.0002 and $1.4414 \pm 0.0002 M_\odot$, respectively.

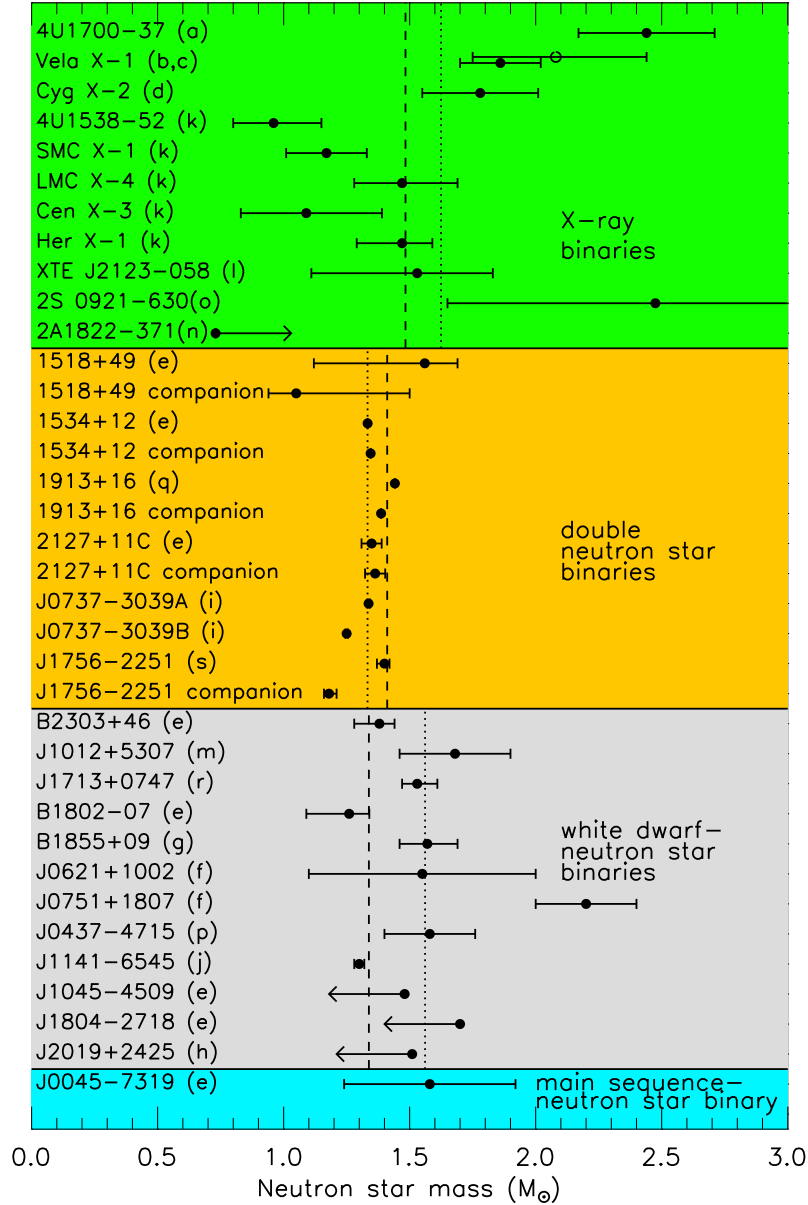


Figure 5.1: Measured and estimated masses of neutron stars in radio binary pulsars (gold, silver and blue regions) and in x-ray accreting binaries (green). Letters in parentheses refer to references cited in Ref. 26.

One particularly significant development is mass determinations in binaries with white dwarf companions, which show a broader mass range than binary pulsars having neutron star companions. It has been suggested that a rather narrow set of evolutionary circumstances conspire to form double neutron star binaries, leading to a restricted range of neutron star masses. This restriction is relaxed for other neutron star binaries. Evidence is accumulating that a few of the white dwarf binaries may contain neutron stars larger than the canonical $1.4 M_{\odot}$ value, including the fascinating case²⁷ of PSR J0751+1807 in which the estimated mass with 1σ error bars is $2.2 \pm 0.2 M_{\odot}$. For this neutron star, a mass of $1.4 M_{\odot}$ is about 4σ from the optimum value. In addition, the *mean* observed value

of the white dwarf-neutron star binaries exceeds that of the double neutron star binaries by $0.25 M_{\odot}$. However, the 1σ errors of all but one of these systems extends into the range below $1.45 M_{\odot}$. Continued observations guarantee that these errors will be reduced. Raising the limit for the neutron star maximum mass could eliminate entire families of EOS's, especially those in which substantial softening begins around 2 to $3n_s$. This could be extremely significant, since exotica (hyperons, Bose condensates, or quarks) generally reduce the maximum mass appreciably.

Masses can also be estimated for another handful of binaries which contain an accreting neutron star emitting x-rays. Some of these systems are characterized by relatively large masses, but the estimated errors are also large. The system of Vela X-1 is noteworthy because its lower mass limit (1.6 to $1.7M_{\odot}$) is at least mildly constrained by geometry²⁸. Mass estimates of selected x-ray binaries are also shown in Fig. 5.1.

5.2. Radii and Redshifts

Most known neutron stars are observed as pulsars and have photon emissions from radio to x-ray wavelengths dominated by non-thermal emissions believed to be generated in a neutron star's magnetosphere. Such emissions are difficult to utilize in terms of constraining the star's global aspects, such as mass, radius and temperature. However, approximately a dozen neutron stars with ages up to a million years old have been identified with significant thermal emissions. Stars of these ages are expected to have surface temperatures in the range of 3×10^5 K to 10^6 K, *i.e.*, they are predominately x-ray sources. If their total photon fluxes were that of a blackbody, they would obey

$$F_{\infty} = L_{\infty}/4\pi d^2 = \sigma T_{\infty}^4 (R_{\infty}/d)^2, \quad (5.1)$$

where, d is the distance, and T_{∞} , F_{∞} and L_{∞} refer to the temperature, flux and luminosity redshifted relative to their values at the neutron star surface. The redshift is $z = (1 - 2GM/Rc^2)^{-1/2} - 1$. (For example, $T_{\infty} = T/(1+z)$, $F_{\infty} = F/(1+z)^2$.) As a result, the so-called radiation radius, $R_{\infty} = R(1+z)$, is a quantity that can be estimated if F_{∞} , T_{∞} and d are known. R_{∞} is a function of both M and R , but if redshift information is available, M and R could be determined. Contours of R_{∞} are displayed in Fig. 4.3. A value of R_{∞} requires both that $R < R_{\infty}$ and $M < (3\sqrt{3}G)^{-1}c^2R_{\infty} \simeq 0.13(R_{\infty}/\text{km})M_{\odot}^{-1}$.

A serious problem in determining R_{∞} and T_{∞} is that the star's atmosphere rearranges the spectral distribution of emitted radiation, *i.e.*, they are not blackbodies²⁹. Neutron star atmosphere models are mostly limited to non-magnetized atmospheres, although pulsars are thought to have intense magnetic fields $\gtrsim 10^{12}$ G. Strongly magnetized hydrogen is relatively simple, but magnetized heavy element atmospheres are still in a state of infancy.

A useful constraint is provided by a few cases in which the neutron star is sufficiently close for detection of optical radiation. These stars are observed to have optical fluxes factors of 3 to 5 times greater than a naive blackbody extrapolation from the x-ray range would imply. This optical excess is a natural consequence of the neutron star atmosphere, and results in an inferred R_{∞} substantially greater than that deduced from the x-ray blackbody. In many cases a heavy-element atmosphere appears to fit the global spectral distributions from x-ray to optical energies while also yielding neutron star radii in a plausible range. However, the observed absence of narrow spectral features, predicted by

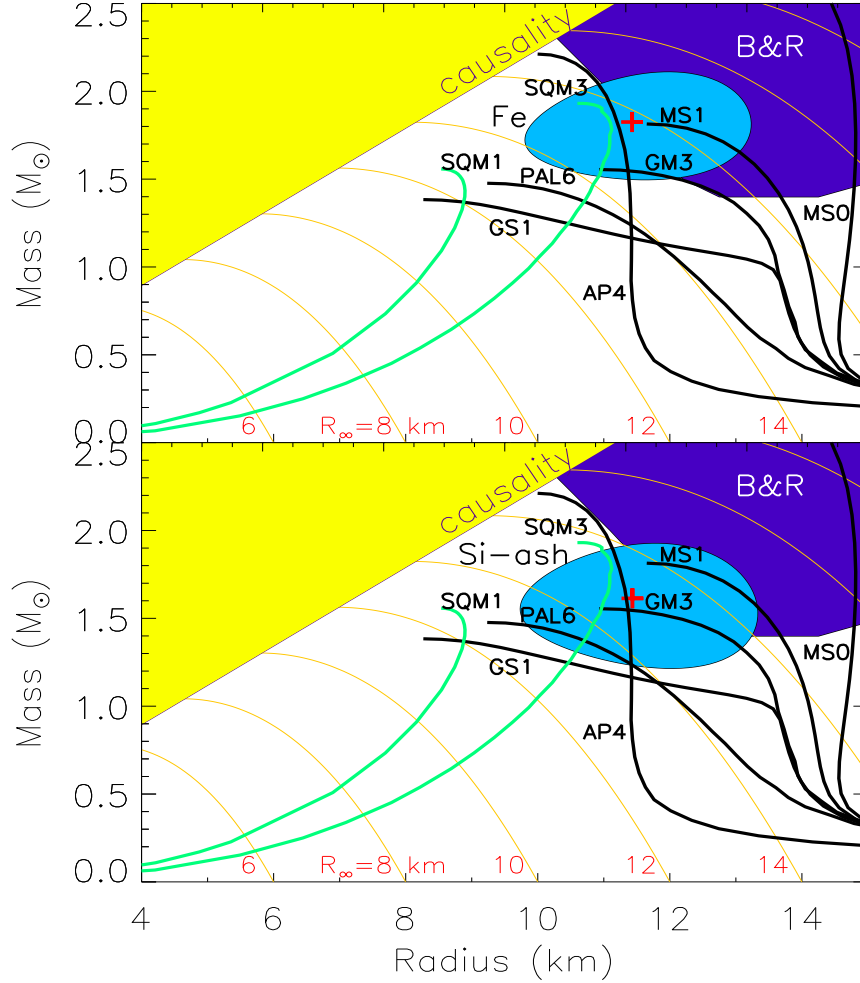


Figure 5.2: Estimated mass and radius for RX J185635-3754 from Ref. 30 and Ref. 31 (dark blue region).

heavy-element atmosphere models, is puzzling. The explanation could lie with broadening or elimination of spectral features caused by intense magnetic fields or high pressures.

The estimation of radii from isolated neutron stars is also hampered by uncertainties of source distance. Distances to pulsars can be estimated by their dispersion measures, but in a three cases (Geminga, RX J185635-3754 and PSR B0656+14) parallax distances have been obtained, although errors are still large. As a consequence, values of R_∞ determined from thermally-emitting neutron stars, while in a plausible range, are not sufficiently precise at present to usefully restrict properties of dense matter. In the case of RX J185635-3754, Walter and Lattimer³⁰ and Braje and Romani³¹ separately deduced values of the neutron star mass and radius shown in Fig. 5.2. These estimates suggest relatively large neutron star radii with $R_\infty > 14$ km begin favored; the canonical $1.4 M_\odot$, 10 km star is disfavored.

5.2.1. Estimates from Quiescent X-ray Bursters in Globular Clusters

In this context, the recent discovery of thermal radiation from quiescent x-ray bursters in globular clusters is particularly interesting. These systems contain rejuvenated 10 billion year-old neutron stars heated by recent episodes of mass accretion from their companions. Since the accreted material was dominated by hydrogen, and accretion is known to quench magnetic fields, these stars may have the simplest of all possible atmospheres: non-magnetic hydrogen. Measurements from the neutron star X7 in the Globular Cluster 47 Tucanae yield $R_\infty \simeq 17.5 \pm 2.5$ km (see Fig. 5.3)³². For $1.4 M_\odot$, this implies a radius range from 12 to 17 km. Accuracy is limited by systematic uncertainties in the intervening interstellar hydrogen column density, since this material obscures 50% or more of the x-ray flux and by the distance to the globular cluster. In addition, although a pure H atmosphere was assumed, small heavy element contamination cannot be ruled out, which would decrease radii. Heavy elements could be present only if accretion was ongoing, but the stability of the observed X-ray flux implies that it is not. Interestingly, the distances to these sources will likely become relatively well known in the near future, reducing a source of error that plagues interpretations of isolated neutron stars.

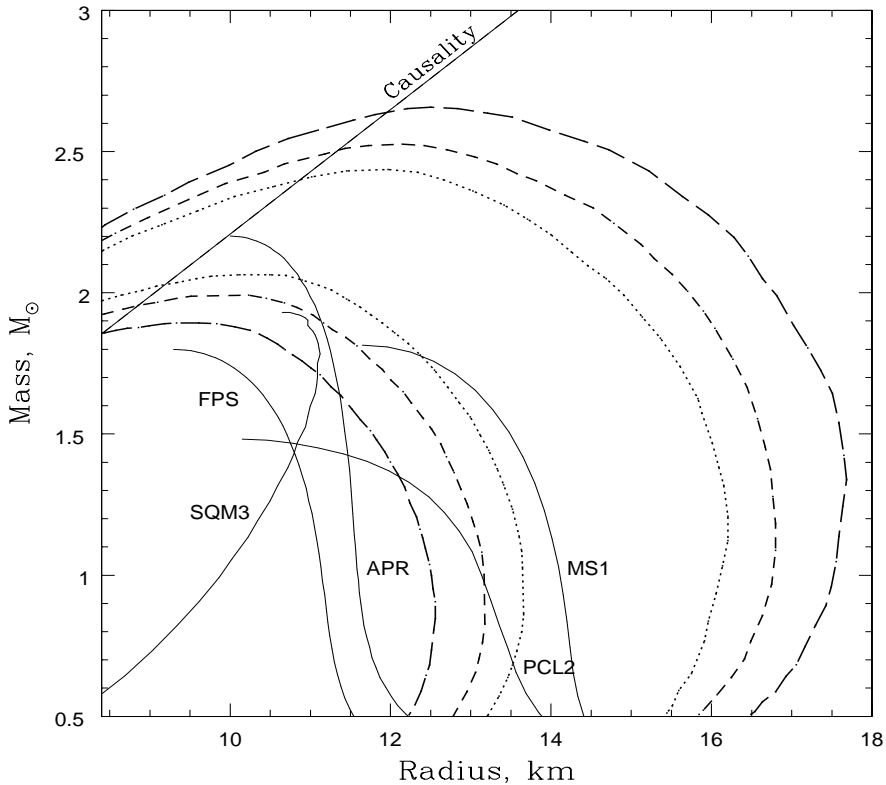


Figure 5.3: Estimated ranges of masses and radii of the neutron stars X7 in 47 Tucanae. Confidence contours are 1-, 2- and 3-*sigma*, respectively, for hydrogen atmosphere models. From Ref. 32.

5.2.2. Estimates from Active X-ray Bursters

Neutron stars that are actively accreting material from companion stars produce x-ray bursts. The resulting light curves can be modelled taking into account light-bending which constrains the star's compactness. For the source XTE J1814-338, Bhattacharyya et al.³³ found $z < 0.38$. For the source 4U 1820-30, Shaposhnikov & Titarchuk³⁴ found $0.20 < z < 0.30$ with a small dependence upon assumed source distance. These estimates are based on a geometric technique and are argued to be insensitive to spectral modelling.

Two lines observed in x-ray burst spectra of EXO 0748-676 have been suggested to be H- and He-like Fe lines and imply $z \simeq 0.35$ ³⁵. This inference received additional credibility by the measurement³⁶ of a 45 Hz neutron star spin frequency. This low spin rate is consistent with the observed equivalent widths of these lines if they are due to Fe and further implies $9.5 < R < 15$ km (corresponding to $1.5 < M < 2.3 M_\odot$). Since this star is a member of an eclipsing binary, an independent mass measurement might yet be possible, which could fix R . These techniques could potentially be extended to other x-ray bursters.

5.3. Pulsar Glitches

Pulsars provide several sources of information concerning neutron star properties. The fastest pulsars provide constraints on neutron star radii. Their spins and spin-down rate provide estimates of magnetic field strengths and ages. A potentially rich source of data are pulsar glitches, the occasional disruption of the otherwise regular pulses. While the origin of glitches is unknown, their magnitudes and stochastic behavior suggests they are global phenomena³⁷. The leading glitch model involves angular momentum transfer in the crust from the superfluid to the normal component³⁸. Both are spinning, but the normal crust is decelerated by the pulsar's magnetic dipole radiation. The superfluid is weakly coupled with the normal matter and its rotation rate is not diminished. But when the difference in spin rates becomes too large, something breaks and the spin rates are brought closer in alignment. The angular momentum observed to be transferred between the components, in the case of the Vela pulsar, amounts to at least 1.4% of the star's total³⁷.

If this also corresponds to the fraction of the moment of inertia residing in the neutron star crust, limits can be set on the star's mass and radius. In terms of the density and pressure n_t and P_t , at the base of the crust, this fraction is³⁷

$$\frac{\Delta I}{I} \simeq \frac{28\pi}{3} \frac{P_t R^4}{GM^2} \frac{1 - 1.67\beta - .6\beta^2}{1 + (2P_t/n_t\beta^2)(1 + 5\beta - 14\beta^2)}. \quad (5.2)$$

The dependence on n_t is weak. P_t and n_t depend on the symmetry energy's density dependence as well as on the incompressibility. Hence, there is a range $0.25 < P_t/(\text{MeV fm}^{-3}) < 0.65$ among published EOS's. For given values of $\Delta I/I$ and M , the smallest R compatible with Eq. (5.2) is obtained employing the largest P_t value in this range. For a $1.4 M_\odot$ star, this leads to the limit shown in Fig. 4.3. This limit has a relatively weak dependence on the EOS ($R \propto P_t^{-1/4}$); however, it applies only to the Vela pulsar, and it depends upon the crustal superfluid coupling hypothesis.

5.4. Moments of Inertia From Relativistic Binaries

It might be possible to measure the entire moment of inertia of a neutron star using pulsar timing in relativistic binaries. Spin-orbit coupling produces two relativistic effects that could be measured: a small extra advance of the periastron of the orbit beyond the standard post-Newtonian advance, and the precession of the pulsar spins about the direction of the total angular momentum of the system, an effect also known as geodetic precession^{39–40}.

Since the total angular momentum remains fixed, the precession of the pulsar spins produces a compensating change in the orientation of the orbital plane. Since the orbital angular momentum dominates the spin angular momenta, the geodetic precession amplitude is very small while the associated spin precession amplitudes are substantial. The spin-orbit effects usually simplify because one star (hereafter called A) spins much faster than the other star B. Then, all observable spin-orbit effects are proportional to the moment of inertia of pulsar A, I_A . To lowest post-Newtonian order, the spin \vec{S}_A and orbital \vec{L} angular momenta evolve according to³⁹,

$$\dot{\vec{S}}_A = \frac{2\pi}{P_{pA}} \frac{\vec{L} \times \vec{S}_A}{|\vec{L}|}, \quad \vec{L} \dot{S}_O = \frac{2\pi}{P_{pA}} \left(\frac{\vec{S}_A}{|\vec{L}|} - 3 \frac{\vec{L} \cdot \vec{S}_A}{|\vec{L}|^3} \vec{L} \right), \quad (5.3)$$

where a and e are the orbital semimajor axis and the eccentricity, respectively, and the precession period P_{pA} and $|\vec{L}|$ are

$$P_{pA} = \frac{2aP(M_A+M_B)c^2(1-e^2)}{GM_B(4M_A+3M_B)}, \quad |\vec{L}| = \frac{2\pi M_A M_B a^2 (1-e^2)^{1/2}}{P(M_A+M_B)}. \quad (5.4)$$

P is the binary orbital period. If θ_A is the angle between \vec{S}_A and \vec{L} , the amplitude of the change in the orbital inclination i due to A's precession is

$$\delta_i = \frac{|\vec{S}_A|}{|\vec{L}|} \sin \theta_A \simeq \frac{I_A (M_A + M_B)}{a^2 M_A M_B (1 - e^2)^{1/2}} \frac{P}{P_A} \sin \theta_A, \quad (5.5)$$

where P_A is A's spin period. This will cause a periodic departure from the expected time-of-arrival of pulses from pulsar A of amplitude (for $e \simeq 0$)

$$\delta t_a = \frac{M_B}{M_A + M_B} \frac{a}{c} \delta_i \cos i = \frac{a}{c} \frac{I_A}{M_A a^2} \frac{P}{P_A} \sin \theta_A \cos i. \quad (5.6)$$

The ratio of the periastron advances due to spin-orbit coupling and to first-order post Newtonian contributions is⁴⁰

$$\frac{A_{pA}}{A_{1PN}} = \frac{I_A (4M_A + 3M_B) P}{6 (1 - e^2)^{1/2} M a^2 M_A P_A} (2 \cos \theta_A + \cot i \sin \theta_A \sin \phi_A), \quad (5.7)$$

where ϕ_A is the angle between the line of sight to pulsar A and the projection of \vec{S}_A on the orbital plane.

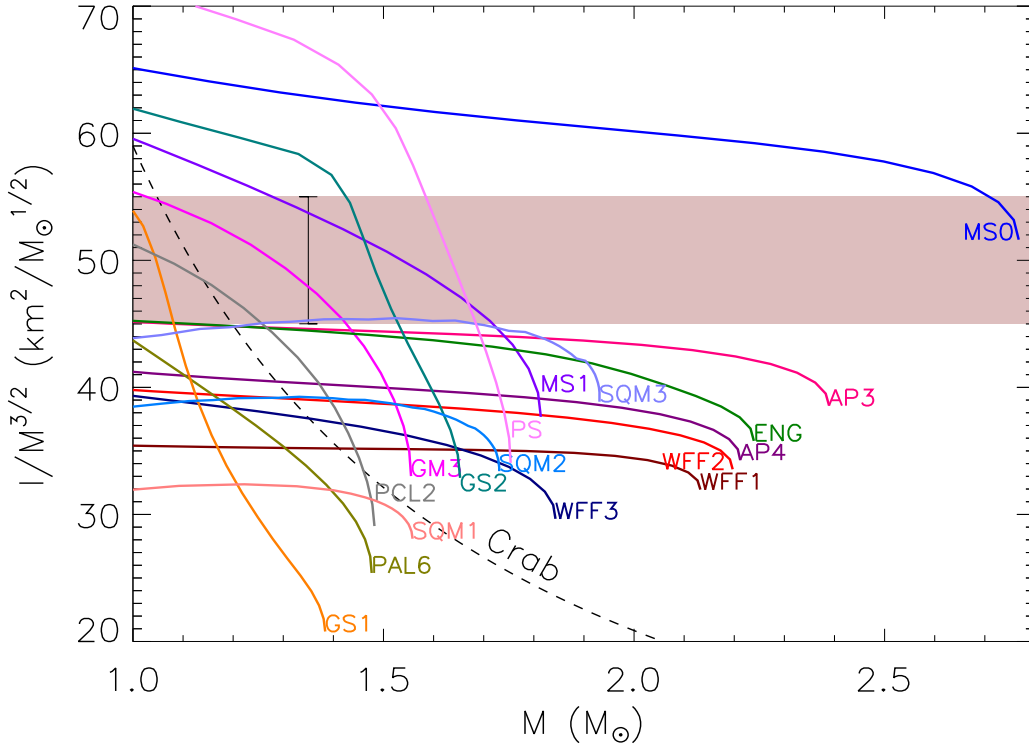


Figure 5.4: The moment of inertia scaled by $M^{3/2}$. EOS labels are described in Ref. 16. The shaded band illustrates a $\pm 10\%$ error on a hypothetical $I/M^{3/2}$ measurement of $50 \text{ km}^2 \text{ M}_{\odot}^{-1/2}$; the error bar is for $M = 1.34 \text{ M}_{\odot}$. The dashed curve labelled Crab is a lower limit for the Crab pulsar.

It is noteworthy that the net timing delays due to inclination shifts due to precession are more than an order of magnitude larger for PSR 1913+16 and PSR 1534+12 than for PSR 0737-3039, due to their smaller inclinations. In particular, PSR 0737-3039 has a nearly edge-on orbit, $i \simeq 90^\circ$, and a small misalignment angle θ_A that make the inclination timing delays extremely small. However, these same attributes render the spin-orbit contribution to the periastron advance about 6 times larger than for the other two systems. Coupled with 0737's shorter precession period, this produces a factor 24 in observability for this effect, which has remained undetectable in other systems. It is expected that I_A can be determined to about 10% after a few years observations¹⁷.

The importance of a measurement of I to within $\pm 10\%$ is illustrated in Fig. 5.4. The curve Crab illustrates a limit for the Crab pulsar⁴¹. It is clear that relatively few equations of state would survive these constraints. Those families of models lying close to the measured values would have their parameters limited correspondingly. Using Eq. (4.14) should then allow a measurement of R , since M is precisely known. For a 1.4 M_{\odot} star, a 10% uncertainty in K would result in a radius estimate with about 6 to 7% uncertainty.

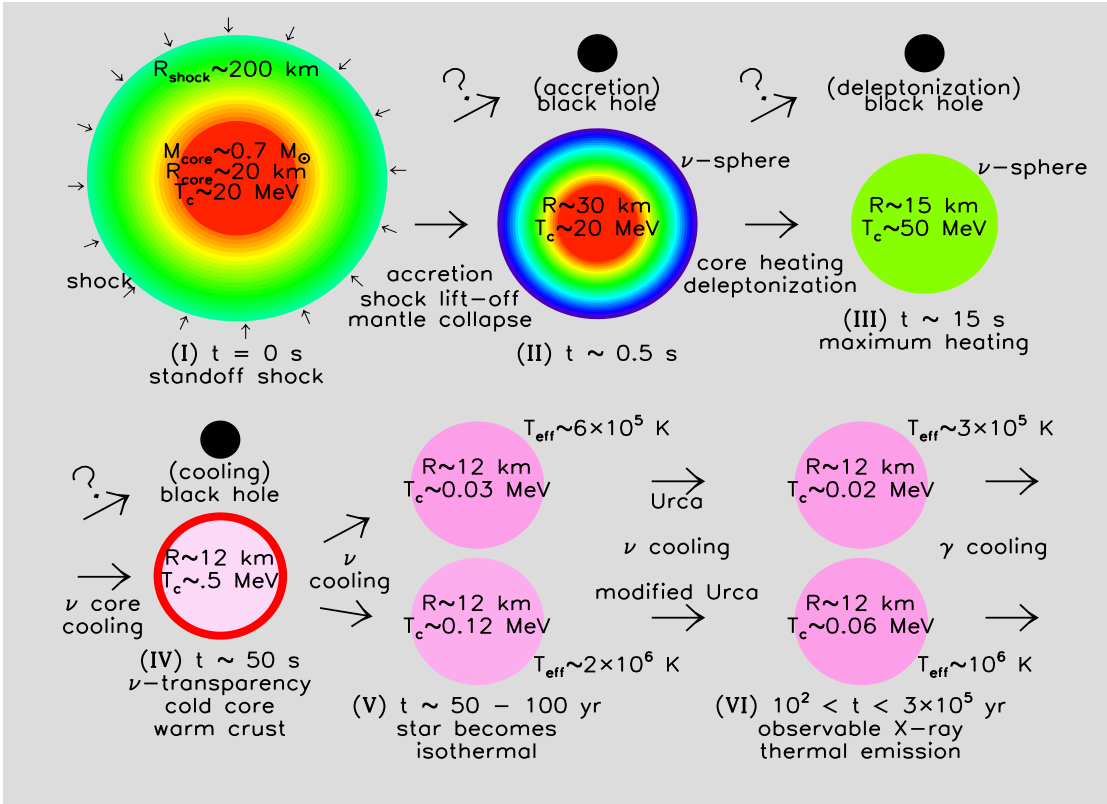


Figure 6.1: The main stages of evolution of a neutron star. Roman numerals indicate various stages described in the text. The radius R and central temperatures T_c for the neutron star are indicated as it evolves in time t .

6. Evolution of Neutron Stars

6.1. Neutron Star Birth

Neutron stars are created in the aftermath of the gravitational collapse of the core of a massive star ($> 8 M_\odot$) at the end of its life, which triggers a Type II supernova explosion. Newly-born neutron stars or proto-neutron stars are rich in leptons, mostly e^- and ν_e . The detailed explosion mechanism of Type II supernovae are not understood⁴², but it is probable that neutrinos play a crucial role.

Core collapse halts when the star's interior density exceeds n_0 , which triggers the formation of a shock wave at the core's outer edge. The shock wave propagates only about 100 to 200 km before it stalls, having lost energy to neutrinos and from nuclear dissociation of the material it has plowed through (stage (I) in Fig. 6.1). Apparently, neutrinos from the core, assisted perhaps by rotation, convection and magnetic fields, eventually resuscitate the shock, which within seconds accelerates outwards, expelling the massive stellar mantle. The proto-neutron star left behind rapidly shrinks due to pressure losses from neutrino emission in its periphery (stage II). The escape of neutrinos from the interior occurs on a diffusion time of seconds. Neutrinos observed from SN 1987A in the Large Magellanic Cloud confirmed this time scale and the overall energy release of $\simeq 3 \times 10^{53}$ ergs^{43–44}.

The loss of neutrinos and lepton number neutronizes the matter. In the core, the $\mu_{\nu e} \sim 300$ MeV but Eq. (1.8) shows that neutrinos escape with $E_{\nu,esc} \sim 20$ MeV. The energy

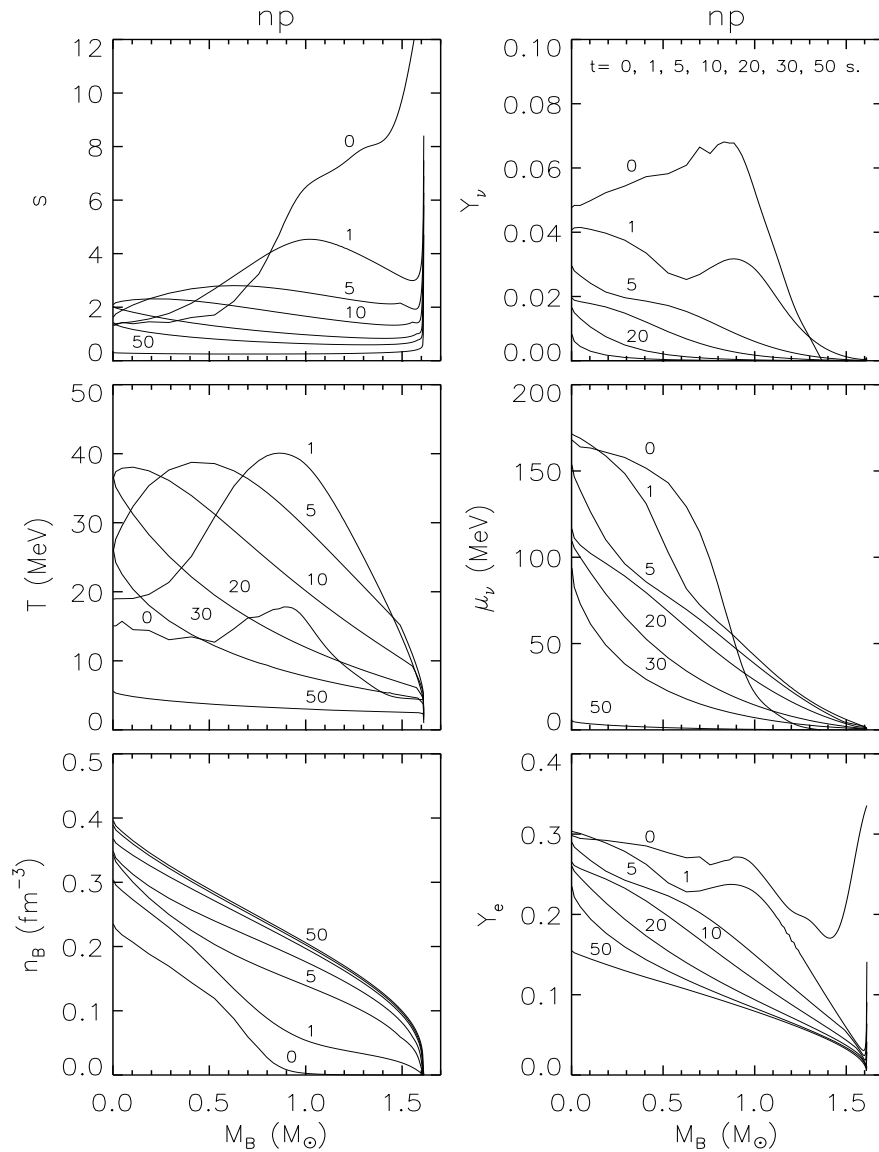


Figure 6.2: Temporal and radial variation of entropy per baryon s , T , baryon density n_B , the net electron neutrino abundance Y_ν , electron neutrino chemical potential $\mu_{\nu e}$, and the net electron concentration Y_e inside a proto-neutron star. Taken from Ref. 45; the simulation uses the EOS GM3 for nucleons-only matter. Labels indicate time in seconds. The abscissa shows the enclosed baryonic mass.

left behind warms the stellar interior (Fig. 6.2), more than doubling the core temperature (stage III), reaching ~ 50 MeV. After 10 to 20 s, however, the steady emission of neutrinos begins to cool the interior⁴⁵. Because the cross section $\sigma \propto \lambda^{-1}$ scales like the square of the mean neutrino energy, the condition $\lambda > R$ is achieved in about 50 s. The star becomes transparent to neutrinos (stage IV), and its cooling rate accelerates.

The proto-neutron star, in some cases, might not survive its early evolution, collapsing instead into a black hole. This could occur in two different ways. First, proto-neutron stars accrete mass which has fallen through the shock. This accretion terminates when the shock lifts off, unless the star's mass has exceeded the theoretical maximum mass. It would then collapse and its neutrino signal would abruptly cease⁴⁶. A second mode of black hole creation is possible⁴⁷ since the maximum mass is enhanced relative to a cold star by extra

leptons and thermal energy. The star's mass might be between the proto-neutron star maximum mass and the cold maximum mass. If so, collapse to a black hole would occur on a diffusion time of 10 to 20 s, longer than in the first case. Perhaps such a scenario could explain the enigma of SN 1987A. The 10 s duration of the neutrino signal confirmed the existence of a proto-neutron star, yet there is no evidence that a neutron star now exists in this supernova's remnant. The remnant's observed luminosity is fully accounted for by radioactivity in the ejected meaning that any contribution from magnetic dipole radiation, expected from a rotating magnetized neutron star, is very small. Either there is presently no neutron star, or its spin rate or magnetic field are substantially smaller than those of typical pulsars. A delayed collapse scenario could account for these observations.

6.2. Neutron Star Cooling

The interior of a proto-neutron star loses energy at a rapid rate by neutrino emission. Within 10 to 100 y, the thermal evolution time of the crust, heat transported by electron conduction into the interior, where it is radiated away by neutrinos, creates an isothermal structure (stage (V) in Fig. 6.1). The star continuously emits photons, dominantly in x-rays, with an effective temperature T_{eff} that tracks the interior temperature but about 100 times smaller. The energy loss from photons is swamped by neutrino emission from the interior until the star becomes about 3×10^5 y old (stage VI).

The overall time that a neutron star will remain visible to terrestrial observers is not yet known, but there are two possibilities: the standard and enhanced cooling scenarios. The dominant neutrino cooling reactions are of a general type, known as Urca processes, in which thermally excited particles alternately undergo beta and inverse-beta decays. Each reaction produces a neutrino or antineutrino, and thermal energy is thus continuously lost.

The most efficient Urca process is the direct Urca process involving nucleons:

$$n \rightarrow p + e^- + \bar{\nu}_e, \quad p \rightarrow n + e^+ + \nu_e. \quad (6.1)$$

This process is only permitted if energy and momentum can be simultaneously conserved. The condition $n_n^{1/3} \leq n_p^{1/3} + n_e^{1/3}$ with $n_p = n_e = nY_e$ requires that the proton to neutron ratio exceeds 1/8, or $Y_e \geq 1/9$, which is far above the value found in neutron star matter in the vicinity of n_0 . However, in a mixture of neutrons, protons and electrons, Eq. (3.1) suggests that the proton fraction Y_e satisfies

$$Y_e \simeq 0.048 \frac{n_0}{n} \left[\frac{E_{sym}(n)}{S_v} (1 - 2Y_e) \right]^3, \quad (6.2)$$

where, typically, $S_v \simeq 30$ MeV. Because Y_e generally increases with density, the direct Urca process might still occur above some density threshold⁴⁸. However, if the direct process is not possible, neutrino cooling must occur by the modified Urca process

$$n + (n, p) \rightarrow p + (n, p) + e^- + \bar{\nu}_e, \quad p + (n, p) \rightarrow n + (n, p) + e^+ + \nu_e, \quad (6.3)$$

in which an additional nucleon (n, p) participates in order to conserve momentum. The modified Urca rate is reduced by a factor of $(T/\mu_n)^2 \sim 10^{-4}$ to 10^{-5} compared to the direct Urca rate, and neutron star cooling is correspondingly slower. The standard cooling

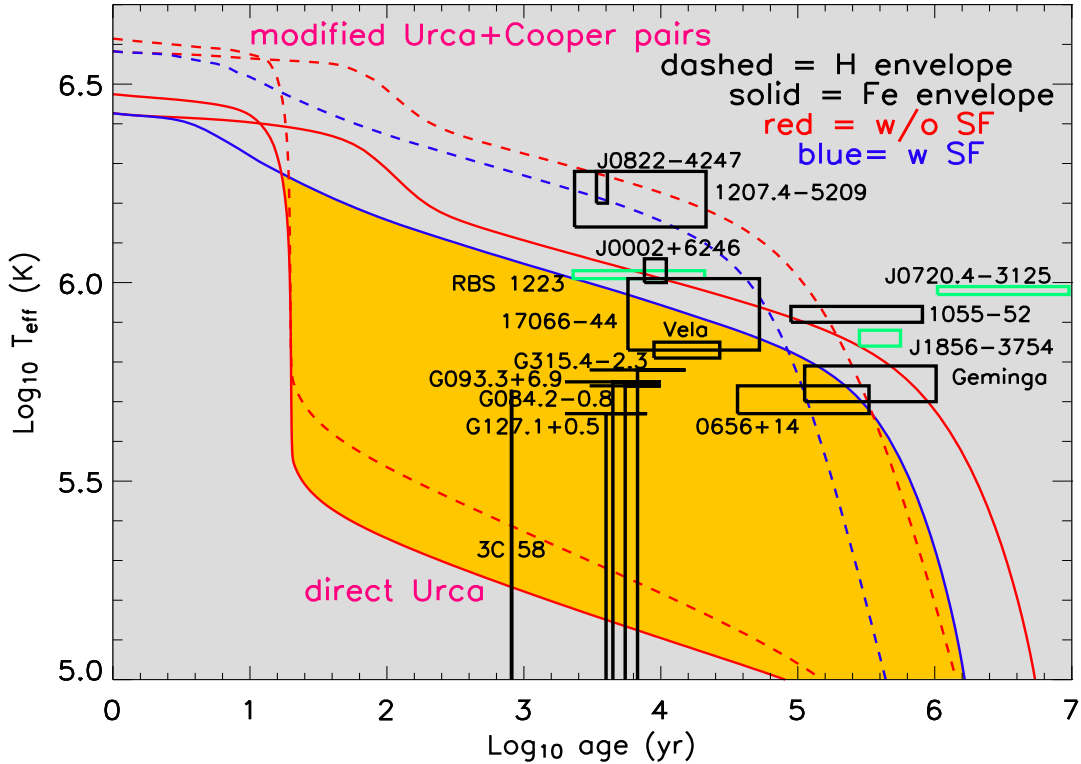


Figure 6.3: Observational estimates (boxes) of neutron star temperatures and ages together with theoretical cooling simulations (curves) for $M = 1.4 M_{\odot}$, described in Ref. 51. Green boxes indicate sources from which both thermal optical and X-ray emissions have been observed. Simulations with Fe (H) envelopes are displayed by solid (dashed) curves; simulations including (excluding) effects of superfluidity are red (blue). The upper four curves include cooling from modified Urca processes only, the lower two curves allow enhanced cooling from direct Urca processes and neglect effects of superfluidity. The yellow region encompasses models with enhanced cooling and superfluidity.

scenario assumes that direct Urca processes cannot occur, and predicts that neutron stars should remain observable by surface thermal emission for up to a few million years.

The question of whether or not the direct Urca process occurs in neutron stars is of fundamental importance. The density dependence of the symmetry energy function E_{sym} determines the values of Y_e and the threshold density at which the nucleonic direct Urca process occurs (see Eq. (6.2)). It also plays an essential role in determining the threshold densities of other particles, such as hyperons, pions, kaons or quarks, whose existences trigger other direct Urca processes⁴⁹. If a star's central density lies below the Urca threshold, enhanced cooling cannot occur. Once again, the quantity $S_v(n)$ plays a crucial role for neutron stars, and its inherent uncertainty means that it is presently unknown if direct Urca processes can occur in neutron stars.

There are two additional issues affecting cooling trajectories of neutron stars: superfluidity and envelope composition. Superfluidity quenches cooling from the direct Urca process. However, an additional cooling source from the formation and breaking of nucleonic

Cooper pairs increases the cooling rate from the modified Urca process⁵⁰. Nevertheless, a clear distinction remains between enhanced and standard cooling trajectories⁵¹.

Envelope composition also plays a role in the inferred surface temperatures. Although it is commonly assumed that the envelope is dominated by iron-peak nuclei, this may not be the case. Light elements (H or He) have smaller photon opacities which enhance surface photon emission. Neutron stars appear warmer with light-element envelopes for their first 100,000 years of cooling but eventually the situation reverses⁵¹.

Theoretical cooling curves can be compared to observations if ages for the thermally-emitting neutron stars can be estimated (Fig. 6.3). The best-determined ages are those for which dynamical information, such as observed space velocities coupled with a known birthplace, is available. Characteristic spin-down ages estimated from pulsar periods P and spin-down rates \dot{P} using $\tau_s = P/2\dot{P}$ are less reliable. In the cases in which both kinds of age estimates are available, they are generally discrepant by factors of 2 to 3.

Theoretical cooling tracks, for a variety of mass, radius and superfluid properties, are relatively narrowly confined as long as enhanced cooling does not occur⁵¹. These tracks are mostly sensitive to envelope composition. When enhanced cooling is considered, cooling tracks fall in a much wider range (yellow region in Fig. 6.3). While most observed stars are consistent with the standard cooling scenario, a few cases for which only upper limits to temperature and luminosity exist may suggest enhanced cooling⁵²; these are shown in Fig. 6.3. Uncertainties in estimated temperature and ages have precluded definitive restrictions on EOS's or superfluid properties from being made.

REFERENCES

1. W. Baade & F. Zwicky, Proc. Nat. Acad. Sci. **20**, 254 (1934).
2. R.C. Tolman, Phys. Rev. **55**, 364 (1939).
3. F. Pacini, Nature **216**, 567 (1967).
4. A. Hewish, S.J. Bell, J.D. Pilkington, P.F. Scott & R.A. Collins, Nature **217**, 709 (1968).
5. T. Gold, Nature **218**, 731 (1968).
6. R.A. Hulse & J.H. Taylor, Ap. J. **195**, 51 (1975).
7. A. Burrows & J.M. Lattimer, Ap. J. **307**, 178 (1986).
8. P.P. Eggleton, J. Faulkner & B.P. Flannery, A & A **23**, 325 (1973).
9. S.M. Johns, P.J. Ellis & J.M. Lattimer, Ap. J. **473**, 1020 (1996).
10. D.G. Ravenhall & J.J. Lattimer, Ap. J. Lett. **223**, 314L (1978).
11. G. Baym, H.A. Bethe & C.J. Pethick, Nucl. Phys. **A175**, 225 (1971).
12. J.M. Lattimer, C.J. Pethick, D.G. Ravenhall & D.Q. Lamb, Nucl. Phys. **A432**, 646 (1985).
13. J.M. Lattimer & F.D. Swesty, Nucl. Phys. **A435**, 331 (1991).
14. D.G. Ravenhall, C.J. Pethick & J.R. Wilson, Phys. Rev. Lett **50**, 2066 (1983).
15. P. Danielewicz, Nucl. Phys. **A727**, 233 (2003).
16. J.M. Lattimer & M. Prakash, Ap. J. **550**, 426 (2001).
17. J.M. Lattimer & B.F. Schutz, Ap. J. **629**, in press; astro-ph/0411470 (2005).
18. H.-A. Buchdahl, Ap. J. **147**, 310 (1967).
19. H. Nariai, Sci. Rep. Gohoku, Univ. Ser. **1** 34 #3, 160 (1950); **35**, 62 (1951).
20. K. Lake, Phys. Rev. D, **67**, 104015 (2003).

21. C.E. Rhoades & R. Ruffini, *Phys. Rev. Lett.* **32**, 324 (1974).
22. J.M. Lattimer, M. Prakash, D. Masak & A. Yahil, *Ap. J.* **355**, 241 (1990).
23. N.K. Glendenning, *Phys. Rev.* **D46**, 1274 (1992).
24. S.L. Shapiro & S.A. Teukolsky, *Black Holes, White Dwarfs, and Neutron Stars* (Wiley: New York, 1983).
25. J.M. Lattimer & M. Prakash, *Science* **304**, 536 (2004).
26. J.M. Lattimer & M. Prakash, *Phys. Rev. Lett.* **94**, 111101(2005).
27. D.J. Nice, E.M. Splaver & I.H. Stairs, in *Binary Radio Pulsars*, eds. F.A. Rasio & I.H. Stairs, *PASP conf. series* (2004).
28. H. Quaintrell et al., *A & A* **401**, 303 (2003).
29. R. Romani, *Ap. J.* **313**, 718 (1987).
30. F. M. Walter & J.M. Lattimer, *Ap. J.* **576**, L145 (2002).
31. T.M. Braje & R.W. Romani, *Ap. J.* **580**, 1043 (2002).
32. G.B. Rybicki, C.O. Heinke, R. Narayan & J.E. Grindlay, *Ap. J.*, in press; *astro-ph/0506563* (2005).
33. S. Bhattacharyya, T.E. Strohmayer, M.C. Miller & C.H. Markward, *Ap. J.* **619**, 483 (2005).
34. N. Shaposhnikov & L. Titarchuk, *Ap. J. Lett.* **606**, 57 (2004).
35. J. Cottam, F. Paerels & M. Mendez, *Nature* **420**, 51 (2002).
36. A.R. Villareal & T.E. Strohmayer, *Ap. J. Lett.* **614**, 121 (2004).
37. B. Link, R.I. Epstein & J.M. Lattimer, *Phys. Rev. Lett.* **83**, 3362 (1999).
38. P.W. Anderson & N. Itoh, *Nature* **256**, 25 (1975).
39. B.M. Barker & R.F. O'Connell, *Phys. Rev.* **D12**, 329 (1975).
40. T. Damour & G. Schaefer, *NuovoCimento* **101B**, 127 (1988).
41. M. Bejger & P. Haensel, *A & A* **405**, 747 (2003).
42. A. Burrows, *Nature* **403**, 727 (2000).
43. A. Burrows & J.M. Lattimer, *Ap. J.* **318**, 63 (1987).
44. J.M. Lattimer & A. Yahil, *Ap. J.* **340**, 426 (1989).
45. J.A. Pons, S. Reddy, M. Prakash, J.M. Lattimer and J. A. Miralles, *Ap. J.* **513**, 780 (1999).
46. A. Burrows, *Ap. J.* **334**, 891 (1988).
47. V. Thorsson, M. Prakash, & J.M. Lattimer, *Nucl. Phys.* **A572** 693 (1994).
48. J.M. Lattimer, C.J. Pethick, M. Prakash & P. Haensel, *Phys. Rev. Lett.* **66**, 2701 (1991).
49. M. Prakash, M. Prakash, J. M. Lattimer & C. J. Pethick, *Ap. J Lett.* **390**, L77 (1992).
50. E. Flowers, M. Ruderman & P. Sutherland, *Ap. J.* **205** 541 (1976).
51. D. Page, J.M. Lattimer, M. Prakash & A.W. Steiner, *Ap. J. Supp.* **155**, 623 (2004).
52. D.L. Kaplan, D.A. Frail, B.M. Gaensler, E.V. Gotthelf, S.R. Kulkarni, P.O. Slane & A. Nechita, *Ap. J. Supp.* **153**, 269 (2004).